



Multiphase evolution of fluids in the Rudnik hydrothermal-skarn deposit (Serbia): new constraints from study of quartz-hosted fluid inclusions

Stefan Petrović¹ · Ronald J. Bakker² · Vladica Cvetković¹ · Rade Jelenković¹

Received: 20 February 2024 / Accepted: 29 April 2024 / Published online: 8 June 2024

© The Author(s), under exclusive licence to Springer-Verlag GmbH Austria, part of Springer Nature 2024, corrected publication 2024

Abstract

This study presents and discusses first detailed petrographic, microthermometric and Raman spectroscopic data from quartz-hosted fluid inclusions at Rudnik Zn-Pb-Cu-Ag skarn deposit (Serbia) and combines them with the information on skarn- and ore paragenesis. Three periods in the metamorphic-hydrothermal history of the deposit are recognized: 1) the pre-ore prograde skarn period when garnet-clinopyroxene skarns formed, 2) the syn-ore period that encompasses a retrograde stage marked by epidote and zoisite and a quartz-sulfide stage characterized by quartz, pyrrhotite, sphalerite, galena and chalcopyrite, and 3) the post-ore period associated with precipitation of calcite and quartz. The hydrothermal evolution is inferred from studying six groups of quartz-hosted fluid inclusions (FI). Two-phase FI of high- (Group A) and moderate salinity (Group B) are found in quartz cores and homogenized at 380–390 °C (mode) and 370–380 °C (mode), respectively. Group A FI consists of H₂O-NaCl liquids and CO₂-CH₄ gas mixtures and likely represents the original fluid composition, whereas Group B FI records dilution of the original fluid at constant temperature, with a slight increase in CH₄ contents. The quartz cores also contain Group C as volatile-rich FI (mostly CO₂ with up to 10 mol% CH₄ and H₂S) of a moderately low salinity and liquid-rich Group D FI composed of pure water with homogenization temperatures of 180–200 °C (mode). The transitional zones of quartz crystals show overgrowth textures and host Group E FI with low salinity that homogenized at 235–401 °C, which vapour phase is a CO₂-CH₄ mixture with up to 17 mol% CH₄. Group F comprises FI found within the rim zones of quartz crystals and they exhibit a low salinity and homogenization temperatures between 259–365 °C. Accordingly, the hydrothermal history at Rudnik involved: a) mixing of different salinity fluids at high temperatures (Groups A and B—retrograde stage), b) introduction of fluids with high volatile contents (Group C) and cooling of fluids with constant salinity (between Groups E and F), which likely correspond to the quartz-sulfide stage, and c) inflow of meteoric water (Group D—the post-ore quartz-calcite stage).

Keywords Skarn deposit · Rudnik · Fluid inclusions · Serbian Cenozoic Magmatic Province · Western Tethyan Metallogenic Belt

Introduction

Skarn deposits represent important sources of W, Sn, Cu, Mo, Fe, Zn, Pb, and may also host economically significant mineralization of Co, Au, Ag, Bi, Be, F, B, U, and REE (e.g. Einaudi et al. 1981; Meinert et al. 2005; Ahmed and Hariri

2006; Chang et al. 2019). These deposits are closely related in time and space to granitoid magmatism of various ages across all continents (e.g. Meinert et al. 2003; Baker et al. 2004; Chang et al. 2019). They are formed by the interaction between a host rock lithology and silicate melt in proximal skarns or hydrothermal fluids in distal skarns (e.g. Meinert et al. 2005). Proximal skarns exhibit a clear spatial relationship between their ore bodies and the parental intrusion, whereas in distal skarns this spatial relationship is only indirectly inferred. In both skarn types, hydrothermal fluids play a significant role in the extraction and transport of metals, therefore, the physicochemical properties of these fluids are important controlling factors for the deposition of base metal-bearing phases (e.g. Kwak 1986; Meinert et al. 2003). Typical high-grade skarns are mostly composed of garnet and pyroxene, both rich Fe, Mg, Al, and Mn, and form by

Editorial handling: F. Lucci

✉ Stefan Petrović
stefan.petrovic@rgf.bg.ac.rs

¹ Faculty of Mining and Geology, University of Belgrade, Đušina 7, 11000 Belgrade, Serbia

² Department of Applied Geosciences and Geophysics, Chair Resource Mineralogy, Montanuniversität, 8700 Leoben, Austria

contact metamorphism of carbonate-rich host rocks. Limestones and dolomites are the most common protoliths for skarns, although skarns are also known to occur in cherts, quartzites and igneous rocks (e.g. Atkinson and Einaudi 1978; Shimazaki 1982; Vidal et al. 1990).

Over the past decades, researchers have focused on various aspects of skarn genesis, such as geodynamic and geochemical conditions of skarn and ore formation (e.g. Meinert et al. 2005; Schwinn et al. 2006; Xie et al. 2018; Chang et al. 2019), understanding the zoning patterns in skarn minerals (e.g. Calagari and Hosseinzadeh 2006; Canet et al. 2011; Zucchi et al. 2023), or unravelling the evolution of ore-forming fluids (e.g. Baker et al. 2004; Samson et al. 2008; Bodnar et al. 2014). Studies of fluid inclusions trapped in rock-forming minerals (e.g., quartz, garnet, calcite or epidote) and sulfides (sphalerite) have particularly contributed to a better understanding of the formation of skarn deposits (e.g. Wilkinson 2001; Baker et al. 2004; Bodnar et al. 2014), revealing that these deposits form under variable pressure and temperature conditions from fluids that also vary in composition (e.g. Roedder 1984; Lattanzi 1991; Lu et al. 2003).

This study focuses on Rudnik polymetallic Zn-Pb-Cu-Ag skarn deposit located in the Serbo-Macedonian Metallogenic Province (SMMP) in central Serbia, which is part of the regional Western Tethyan Metallogenetic Belt (Fig. 1a; Janković 1990). The deposit has been mined industrially since 1950 and represents an important regional source of metals with to date production of ~13 million of metric tons of polymetallic ore (Popović and Umeljić 2015). The average contents of metals in skarn ore in Rudnik ranges widely for Pb (0.94–5.66 wt%), Zn (0.49–4.49 wt%), Cu (0.08–2.18 wt%), and Ag (50–297 µg/g) (Stojanović et al. 2018). Despite the significant geological data obtained through half a century of industrial exploration, there are to date just a few detailed scientific studies about the Rudnik deposit (e.g. Cvetković et al. 2016a; Stojanović et al. 2018; Kostić et al. 2021). The existence of only preliminary studies on fluid inclusions (Blečić 1974; Tošović 2000), significantly hinders more advanced genetic considerations on the origin of this deposit. In this study, we use microthermometry and Raman spectroscopy on fluid inclusions in rock and ore-related hydrothermal quartz in order to characterize the fluids associated with the ore formation. By combining these data with the information on skarn and ore petrography we try to better constrain the temporal context of hydrothermal evolution and clarify physiochemical conditions during the ore formation.

Geological setting

Ore deposits in Serbia belong to the regional Western Tethyan Metallogenetic Belt, or the Alpine-Balkan-Carpathian-Dinaride metallogenic and geodynamic province, which is

part of the Alpine-Himalayan orogenic system that extends from Western Europe to Southeast Asia (Janković 1990; Heinrich and Neubauer 2002). The geodynamic evolution of the Western Tethyan Metallogenetic Belt broadly occurred from the Late Jurassic to the Late Cretaceous (e.g. Ustaszewski et al. 2010; Gallhofer et al. 2015; Cvetković et al. 2016b) and involved the formation of numerous and significant mineral deposits in SE Europe (Melcher and Reichl 2016). Metallic mineral deposits in Serbia are present in four regional metallogenic units (Fig. 1a): the Dinaridic metallogenic province (DMP), the Serbo-Macedonian metallogenic province (SMMP), the Carpatho-Balkan metallogenic province (CBMP), and the Dacian metallogenic province (DcMP); they are subdivided into several metallogenic zones, ore districts and ore fields (Jelenković 2014).

The Rudnik ore deposit is located in the central part of the SMMP known as the Šumadija metallogenetic zone. The SMMP ore deposits are spatially and temporally associated with Oligocene and Miocene magmatism (e.g. Palinkaš et al. 2013; Šošarić et al. 2013; Cvetković et al. 2016a; Hoerler et al. 2022) that occurred during the transition from collision to post-orogenic extension (late Eocene-early Miocene), roughly between 35 and 20 Ma, pre-dating widespread Miocene extension-related magmatism in the Pannonian Basin (Seghedi et al. 2004; Richards 2015). These Cenozoic magmatic rocks intrude or overlie the basement composed of Mesozoic ophiolites and flysch sediments of the Vardar zone, metamorphic crystalline of the European derived units and limestones of the Adria derived units (Janković, 1990; Heinrich and Neubauer 2002).

The SMMP comprises numerous hydrothermal vein-, skarn-, carbonate replacement-, locally porphyry-type ore deposits in Serbia, with a predominant Pb, Zn, Sb, Bi, Ag, and As metals, and the subordinate occurrence of Cu, Au and Mo. The Šumadija metallogenetic zone is considered as a Pb–Zn–Ag dominant region of the entire SMMP (Jelenković et al. 2008).

Geology of the Rudnik deposit

On the map (Fig. 1b), the Rudnik volcano-intrusive complex is an NNW-SSE elongated area, consisting mainly of two large masses of volcanic and shallow intrusive facies and a skarn deposit located between them (Cvetković et al. 2016a). The basement of the volcano-intrusive complex consists of Cretaceous (Barremian-Aptian and Turonian-Senonian) flysch sediments, whereas farther from the deposit, similar volcanic rocks are spatially associated with Oligocene and Miocene sediments (Filipović et al. 1978).

The local geology of the Rudnik deposit includes Jurassic ultramafic rocks overthrust by Upper Cretaceous flysch sediments; both are crosscut and/or overlain by acid to

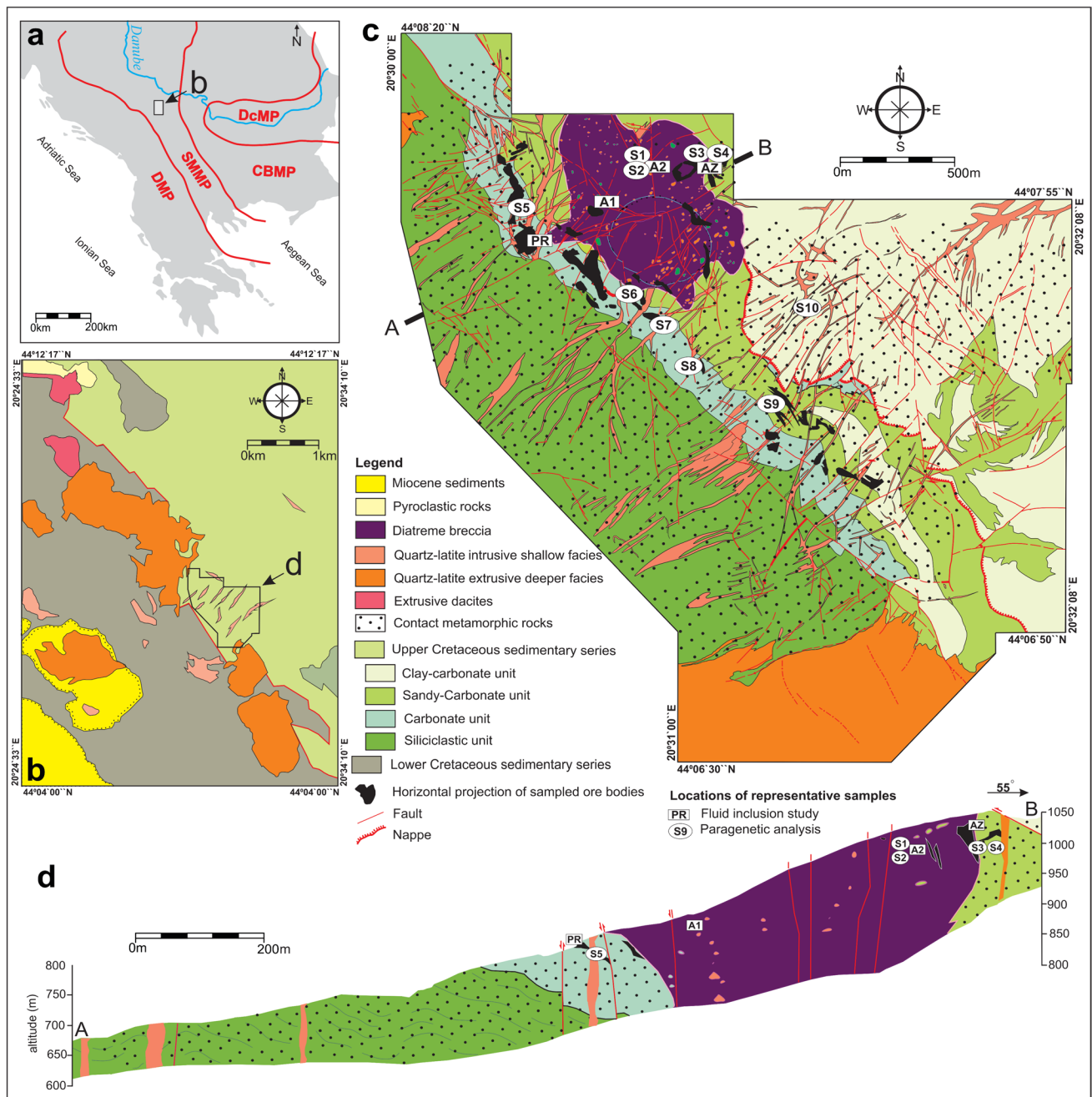


Fig. 1 a Metallogenetic provinces of southeastern Europe: DMP-Dinaridic, SMMP-Serbo-Macedonian, CBMP-Carpatho-Balkan DcMP-Dacian, modified after Dimitrijević (2000) and Melcher and Reichl (2016). b Simplified geological map of the wider area of the

Rudnik deposit, modified after Filipović et al. (1978) and Cvetković et al. (2016b). c, d Geological map and profile of the Rudnik deposit with sample locations modified after Djoković (2013)

intermediate Oligocene and Miocene intrusive and volcanic rocks (Fig. 1c, d; Djoković 2013).

The ultramafic rocks are part of an ophiolite mélangé and are only identified by drilling. These rocks are hydrothermally strongly altered to talc, while partially fresh rocks are present only in the shallower zones of the deposit; they are composed of harzburgites that exhibit typical deformation

features of residual mantle harzburgites (Petrović and Batočanin 2019).

The Upper Cretaceous flysch sediments consist of siliciclastic, limestone, sandy-carbonate, and clay-carbonate concordant units; all units are contact metamorphosed but with recognizable protoliths. The oldest is the siliciclastic unit, which predominantly consists of conglomerate and

sandstone sequences with sporadic intercalations of carbonate breccias and limestone lens-like bodies. The conglomerates have poorly sorted quartz clasts and a sandy matrix, while the sandstones are characterized by horizontal lamination. The overlying limestone unit extends from SE to NW of the deposit, and it hosts the majority of ore bodies in the deposit. It comprises individual olistolithic limestone blocks cemented by a heterogeneous matrix (limestone clastites, marl and fine-grained volcanoclastics). The limestone blocks are crumpled, fractured, without visible layering and elements characteristic of other Upper Cretaceous flysch units. The overlying sandy-carbonate unit comprises sandstones and microconglomerates, as well as marly limestones and siltstones. The clastic rocks are thin-bedded and poorly graded, while the marly limestones occur as lenticular or thick-banked bodies up to hundreds of metres in length between them. In the NE of the deposit, this unit is in tectonic contact with the uppermost clay-carbonate unit, consisting of siltstones and sandstones that alternate rhythmically with thinly layered greyish limestone.

The Upper Cretaceous flysch sediments described above are intruded and/or overlain by Cenozoic volcano-intrusive rocks that formed during two magmatic phases. The Oligocene phase (~30 Ma) is represented by extrusive and shallow intrusive dacites and andesites, whereas the Miocene (~23 Ma) phase produced a wide range of volcanogenic and intrusive facies of quartz-latitude composition; the latter phase is interpreted as petrogenetically linked to the Rudnik deposit (Cvetković et al. 2016a). The Miocene extrusive facies are present in the NW and SW parts of the magmatic complex, whereas their shallow intrusive facies in the form of up to a few tens of meters thick dykes and sill-like bodies as well as diatreme magmatic-hydrothermal breccias occur in the central area, i.e., where the Rudnik deposit is located. The diatreme facies appear as polymict breccias composed of fragments of Upper Cretaceous sedimentary rocks, quartz-latitude, metamorphic rocks, and rare ultramafic rocks enclosed by matrix made up of commonly silicified, clay-marl and/or carbonate material.

The contact metamorphic rocks occupy an area of ~3 km² located in-between the two major extrusive bodies of Miocene quartz-latitude. It hosts all the shallow intrusives of the Rudnik complex as well as all the ore bodies discovered so far. (Fig. 1c). The contact metamorphism was induced by heat and fluids from an inferred granitoid body intruded at the base of the deposit (Djoković 2013; Cvetković et al. 2016a). The contact metamorphic rocks encompass skarn, metasandstone, metamudstone, skarnoids and hornfels, all of which originate from the Upper Cretaceous flysch sediments protoliths. Accordingly, the sandstone and marly-clayey members of the flysch sediments were metamorphosed into metasandstone, metamudstone, and hornfels, and the limestones

were metamorphosed into skarns and skarnoids. Due to a distinctive lithological heterogeneity of the Upper Cretaceous flysch protolith, systematic change in metamorphic mineral assemblages is merely absent, hence only a general pattern in distribution of contact metamorphic facies exists. Epidote-zoisite skarn predominates in metamorphosed carbonates that host primary sulfide mineralization, while garnet-pyroxene skarn occurs in deeper parts of the deposit as the result of contact metamorphism of siliciclastic rocks. The skarns are classified as Ca skarns, among which epidote-zoisite and garnet-pyroxene skarns predominate (Milovanović 2009). Djoković (2013) argues that skarns with dark colored garnet and light colored pyroxene are present in the deeper zones, whereas those having light colored garnet and dark colored pyroxene are more prevalent in shallower zones of the deposit. In general, garnets from Rudnik skarns range in composition from grossular to andradite and their pyroxene corresponds to diopside (Kostić et al. 2021). Epidotite, marble and garnetite are sporadically present as products of contact metamorphosed sandy and marly clay members of Upper Cretaceous flysch series.

Most polymetallic Zn-Pb-Cu-Ag ore bodies in Rudnik are located along the contact between larger quartz-latitude dykes and metamorphosed Upper Cretaceous flysch sediments. The ore is prevalently hosted in epidote-zoisite skarns in a relatively shallow zone up to 300 m from the ground surface, usually in the form of pseudo-layers, nests, veins and lenses (Popović and Umeljčić 2015). More rarely, the ore bodies are found in diatreme breccias, where they have a more irregular geometry, usually as cone-shaped forms that extend upwards over a vertical interval of ~100 m. The sulfide mineralization is predominantly associated with quartz and calcite, and commonly appears in form of stockworks and impregnations, more rarely as massive ore precipitated within the carbonate cement. The size of the ore bodies usually varies from 30–150 thousand tons to the biggest ones that amount to 300–900 a thousand tons of ore. Pyrrhotite is the most abundant sulfide mineral in the deposit and is accompanied by other ore-minerals: sphalerite, galena, chalcopyrite, gangue arsenopyrite, and pyrite (Stojanović et al. 2016).

Sampling and methods

Sampling and thick section preparation

A total of 30 samples are collected, out of which 14 representative samples are selected for further fluid inclusion study and paragenetic analysis. Samples for the fluid inclusion study are collected from the underground exposures of Azna (ore bodies AZ and Z) and surface outcrops of

Prljuša ore zones in the northwestern part of the Rudnik deposit (Fig. 1c, d); at both localities, quartz is common and in association with rock and ore forming minerals. The fluid inclusion study is performed on four selected representative quartz samples (labelled PR, A1, A2 and AZ) associated with macroscopically visible mineralization. The paragenetic relationships between rock- and ore-forming minerals are studied in selected samples taken from underground exposures in different areas and units of the deposit (Fig. 1c). A list of all representative samples with their sampling locations is provided in the Appendix 1. Fluid inclusions are studied from ~150 µm thick double-polished sections prepared at the University of Belgrade, Faculty of Mining and Geology.

Petrography and SEM–EDS study

Rock and ore-forming minerals petrography was performed at the University of Belgrade, Faculty of Mining and Geology, using Olympus BX51 and Zeiss Axio Imager 2 microscopes for transmitted and reflected light microscopy, respectively. The rock samples underwent analysis using a scanning electron microscope (SEM, JSM–6610LV, JEOL Inc., Tokyo, Japan) at 20 kV at the Laboratory for SEM, Faculty of Mining and Geology, University of Belgrade. Mineral associations were determined by analyzing their composition through energy-dispersive X-ray spectrometry (EDS, Xplore 30 by Oxford Instruments, UK), employing internal standards with a detection limit of ~0.1 wt%. Additionally, homogeneity and potential zoning were analyzed using backscattered electron (BSE) micrographs provided in the Appendix 2.

Petrography and microthermometry of fluid inclusions

These investigations are conducted at the Department of Applied Geosciences and Geophysics, Chair of Resource Mineralogy at the Montanuniversity of Leoben (Austria) and at the Fluid inclusion Laboratory at the Faculty of Mining and Geology of the University of Belgrade (Serbia). In Leoben, the fluid inclusions are analysed using a Linkam MDS 600 heating-freezing stage mounted on an Olympus BX 60 optical microscope. Calibration is carried out using synthetic fluid inclusions with three invariant temperatures: the melting point of CO₂ at –56.6 °C, the melting of H₂O ice at 0.0 °C, and the critical homogenization temperature of water at 374.0 °C. The instrument resolution is 0.1 °C, and the standard deviation in each measurement is ±0.2 °C in the range of -150 to +100 °C. Petrographic study was carried out at the University of

Belgrade, Faculty of Mining and Geology, using an Olympus BX51 transmitted-light microscope.

Raman spectroscopy

Raman spectroscopy has been used to identify fluid, solid and gases phases in defined petrography fluid inclusions types. A LabRAM HR Evolution confocal Raman spectrometer (HORIBA, Jobin Yvon GmbH) equipped with an OLYMPUS light microscope is used to record the Raman spectra. The emission line of a HeNe laser (632.817 nm, 17 mW) and an air cooled frequency doubled Nd:YAG laser (532.06 nm, 100 mW) are used for excitation. The remaining power of the Nd:YAG laser at the sample after passing the optics of the Raman spectrometer is about 1 to 1.5 mW. The single stage spectrometer is an 800 mm focal length Czerny-Turner type spectrograph, equipped with 1800 gr/mm and 600 gr/mm (gratings), an Edge filter, and a multichannel air cooled (-70 °C) CCD detector (1024×256 pixels, open electrode front illuminated chip). The spectral resolution is 0.30 to 0.19 cm⁻¹ per pixel at a Raman shift of 100 to 3500 cm⁻¹, respectively, with a 1800 gr/mm and 633 nm laser. Spatial resolution is downsized to a minimum of 2 µm in the confocal mode with an Olympus 100× objective (plan achromatic, n.a. 0.7). The wavenumbers are calibrated with the Rayleigh scattering (0 cm⁻¹), and a silicon wafer (520.7 cm⁻¹). In addition, the presence of specific salt-hydrates and the detection of eutectic melting behaviour are analysed with cryo-Raman spectroscopy, by attaching a Linkam TMS94 heating-freezing stage (Bakker 2004; Baumgartner and Bakker 2010).

Fluids properties computer programs

Salinity, molar volume (density), and pressure of homogenization are calculated using AqSo-NaCl software (Bakker 2018, 2019). The software LonerB and LonerAP (Bakker 2012) are used to perform calculations of densities and liquid–vapour equilibria.

Results

Mineral paragenesis of skarn and sulfide mineralization

The selected skarn samples mostly correspond to epidotezoisite and garnet-clinopyroxene skarns (Fig. 2a, b), which are composed of epidote, coisite, quartz, calcite and actinolite (low-temperature or retrograde skarns) as well as of garnet, quartz, calcite and clinopyroxene (high-temperature or prograde skarns). It is noteworthy that the low-temperature hydrous skarn minerals are usually

spatially associated with sulfide minerals and are sometimes found overprinting high-temperature anhydrous minerals of high-temperature prograde skarns. The sulfide minerals are mainly composed of pyrrhotite, sphalerite, galena, chalcopyrite, pyrite and arsenopyrite, among which pyrrhotite is most abundant in massive, vein or disseminated sulfide mineralization. Polymineral sulfide aggregate is often intergrown with quartz and cemented by quartz-calcite mineral association (Fig. 2c, d). The mineral parageneses are illustrated in Fig. 5, while the chemical composition of the main mineral phases is given in Appendix 2.

Prograde skarn

Garnet is most abundant in the high-temperature skarn paragenesis, often making up over 50 vol% of the rock. It forms small, dark-brownish hypidiomorphic grains (<0.1 mm) arranged as larger porphyroblasts sometimes reaching >2 mm in diameter (Fig. 3a, b). The largest, well-developed garnet crystals often show anisotropy and zonal structure (Fig. 3c), with a prevailing andraditic composition and minimal presence of the grossular component.

Fine-grained aggregates of calcite and quartz occur in cracks or appear as irregularly shaped or a few mm long elongated interstices between garnet crystals (Fig. 3c). The least abundant mineral in the prograde skarn is clinopyroxene augite, which occurs in tiny idiomorphic crystals (<0.1 mm) spatially associated with garnets (Fig. 3b). Ore minerals, usually arsenopyrite, rarely comprise more than 5 vol% and are found inside finely recrystallized calcite in-between garnet crystals, and in calcite (Fig. 3a).

Retrograde skarn

Epidote and zoisite are the most abundant minerals in low-temperature skarn. They often form intergrowths and together amount up to 60 vol% with the prevalence of epidote that sometimes reaches 90 vol%. (Fig. 3d). Epidote most commonly occurs in tiny isometric crystals (<0.5 mm in diameter) and as elongate radial crystals (>0.5 mm in length, Fig. 3d). Zoisite has idiomorphic crystals over 1 mm in length, which sometimes build nests or irregularly shaped aggregates in association with sulfide minerals (Fig. 3e). Actinolite is usually found in retrograde skarn and rarely in prograde skarn. It forms tiny (<0.2 mm in length) fibrous

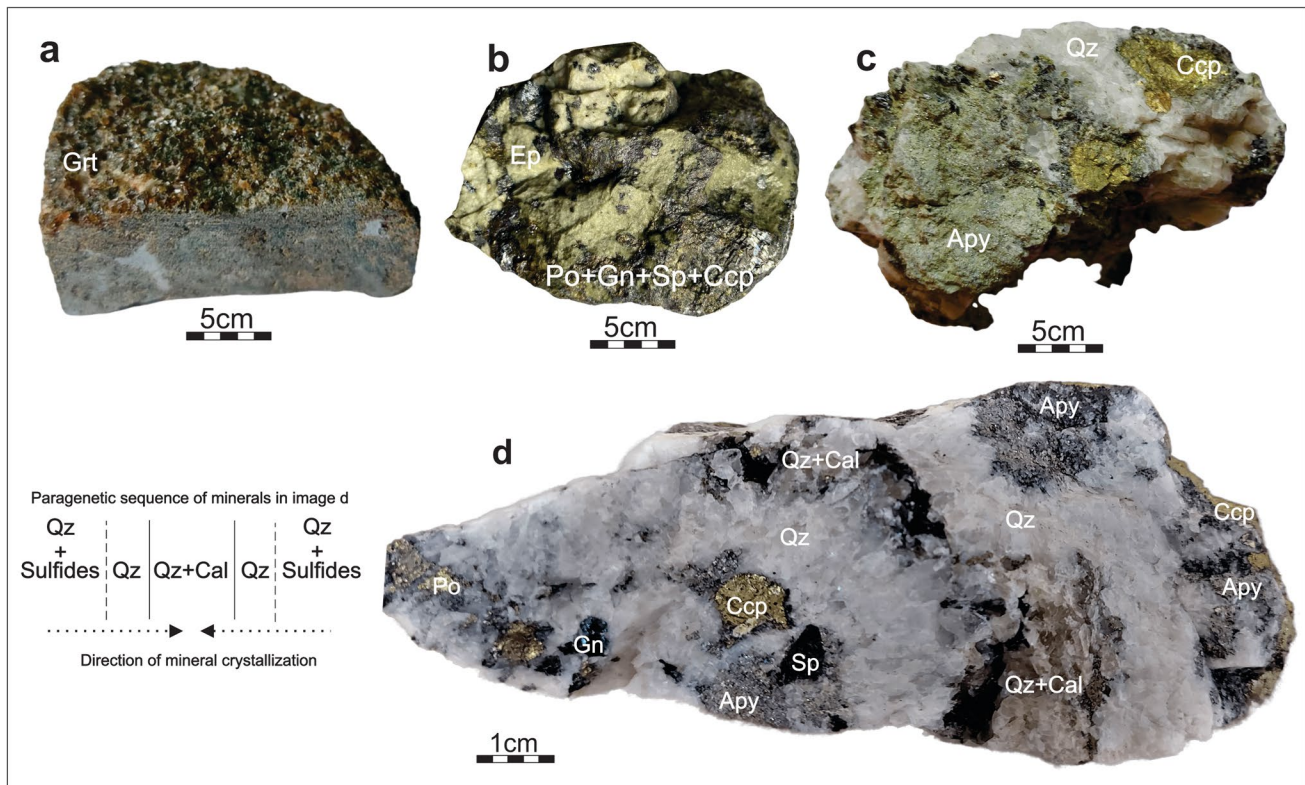


Fig. 2 Representative hand specimens of the main rock types of the Rudnik deposit. **a** Prograde skarn with garnet (grossular-andradite) and clinopyroxene (augite). **b** Mineralized (polymineral aggregate of pyrrhotite, chalcopyrite, sphalerite and galena) epidote-rich skarn **c**, **d**

Ore sample with pyrrhotite, arsenopyrite, chalcopyrite, sphalerite and galena intergrown with quartz. Abbreviations (Whitney and Evans 2010): Apy-arsenopyrite, Cal-calcite, Ccp-chalcopyrite, Ep-epidote, Grt-garnet, Gn-galena, Po-pyrrhotite, Qz-quartz, Sp-sphalerite

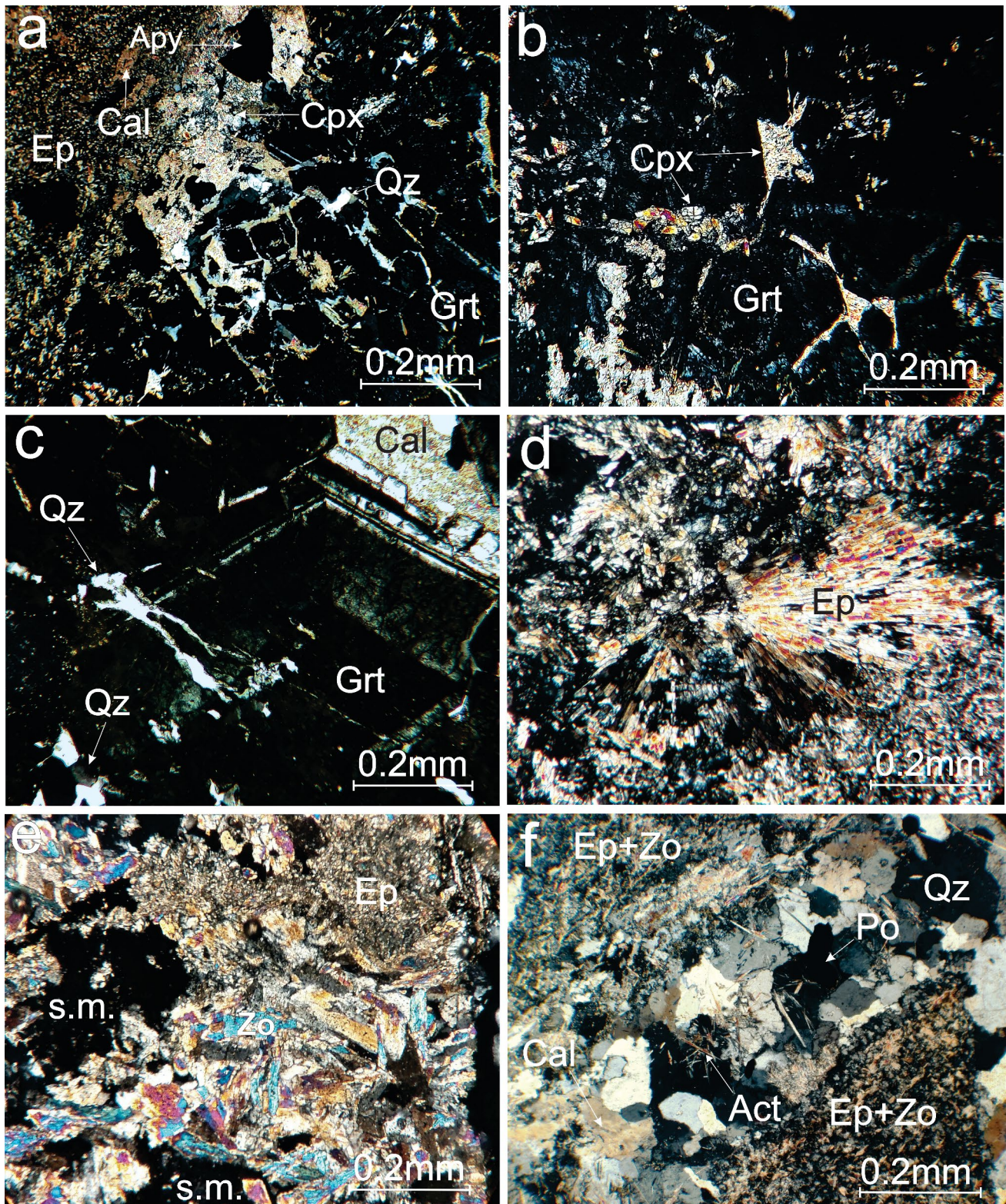


Fig. 3 Photomicrographs (a-f: transmitted-light) of rock-forming minerals from the Rudnik deposit. **a** High-temperature prograde paragenesis (garnet and clinopyroxene) partially replaced by low-temperature retrograde paragenesis (epidote, calcite, quartz) and sulfide minerals (arsenopyrite). **b** Garnet with clinopyroxene in prograde skarn. **c** Quartz and microcrystalline calcite filling cracks within zoned gar-

net in prograde skarn. **d** Epidote pinnate radial crystals in retrograde skarn. **e** Epidote-zoisite intergrowths in retrograde skarn partially replaced by sulfide minerals (s.m.). **f** Quartz vein in prograde skarn replaced by actinolite and pyrrhotite in prograde skarn. Abbreviations: Act-actinolite, Apy-arsenopyrite, Cal-calcite, Cpx-clinopyroxene, Ep-epidote, Grt-garnet, Po-pyrrhotite, Qz-quartz, s.m.-sulfide minerals, Zo-zoisite

crystals that are unevenly distributed in the rock (Fig. 3f). Quartz occurs in small hypidiomorphic (< 1 mm in diameter) or idiomorphic crystals (> 2 mm in diameter) that packed with calcite forming a mosaic (Fig. 3f). Calcite is predominantly fine-grained calcite (< 0.5 mm) and always accompanies ore minerals, whereas coarse-grained calcite crystals are subordinate.

Quartz-sulfide association

The quartz-sulfide mineral association is relatively evenly present in epidote-zoisite skarn and may approach to 30 vol% of rock or forms a massive ore mineralization (Fig. 2b, c, d). Arsenopyrite and pyrite form veins that crosscut the older rock-forming minerals and are cemented by younger pyrrhotite, sphalerite, galena or chalcopyrite (Fig. 4a, b). Pyrrhotite is the most common sulfide mineral, comprising over 50 vol% of the total sulfides, and it exhibits intergrowths with galena, sphalerite, and chalcopyrite in major polymineralic ore-sulfide aggregates (Fig. 4c, d). In the polymineralic aggregates, sphalerite and galena are evenly present (10–40 vol%), while chalcopyrite is subordinate (10–20 vol%) and occurs also as lamellae and point exsolutions within sphalerite (Fig. 4c). Quartz frequently forms intergrowths with all sulfide minerals (Fig. 4c, d), and also appears as white-colored crystals 0.2–10 mm in length or within quartz veins. In these veins, one often encounters subparallel arrays of euhedral quartz crystals, reaching up to 5 cm in length and forming distinctive comb patterns (Fig. 2d).

Quartz-calcite association

The quartz-calcite association is most commonly present in the form of accumulations that cement previously formed sulfide mineralization. Quartz is pale yellow to colorless, rarely forming macroscopically visible crystal forms, and is intergrown with calcite and cements previously formed sulfide minerals (Fig. 2d). Calcite is predominantly fine-grained (< 0.5 mm) and is mosaically 'packed' with quartz within veins that often crosscut epidote-zoisite skarn (Fig. 4e, f).

Petrography of the quartz samples and fluid inclusions

Quartz is present in all periods of the deposit (Fig. 5). In sample PR, quartz occurs in well-developed prismatic crystals that precipitated in the voids between skarnized fragments in breccias. Individual quartz crystals are up to 10 cm in length, with macroscopically visible growth zones (Fig. 6a, e, f). Sample A2 has smaller quartz crystals (< 1 cm) within massive ore mineralization, whereas in sample A1, quartz crystals are anhedral and fill the open space in-between ore mineralization

(Fig. 6b, c). Sample AZ contains idiomorphic quartz crystals up to 2 cm in diameter that occur between massive aggregates of ore minerals (Fig. 6d).

Fluid inclusion assemblages in sample PR occur within three different crystal growth zones (Fig. 7). The core zone contains four types of fluid inclusions: 1) type PRa—up to 50 µm in diameter, semi-irregularly shaped fluid inclusions that compose small groups of usually two to three inclusions with the volume fraction of the vapour phase varying 20–30 vol%. 2) type PRb—fluid inclusions in trails that reflect partly healed cracks and internal growth zones; they are up to 20 µm in size and have a regular or, locally, negative-crystal shape and their volume fraction of the vapour phase varies 50–60 vol%. 3) type PRc—regular or, locally, negative-crystal shaped fluid inclusions, up to 10 µm in size that are extremely rich in vapour phase amounting to 90 vol%; only a few inclusions of this type are observed in the crystal core. 4) type PRd—elongated to irregularly shaped fluid inclusions that occur in trails (healed cracks) usually in the crystal core; they are up to 50 µm in length, liquid-rich or totally liquid. Transition crystal zone contains abundant fluid inclusions of type PRe; they have irregular shapes often elongated exhibiting an orientation perpendicular to the crystal growth direction; these fluid inclusions range 50–300 µm in length and their volume fraction of the vapour phase varies between 10 vol% and 20 vol%. The crystal rim contains traces of growth zones with PRf type of fluid inclusions; they are regularly shaped with an average length of 30 µm, and the volume fraction of the vapour phase varies 20–30 vol%.

Similar to sample PR, in sample A1, three growth zones of quartz crystals are visible (Fig. 7). The core zone contain three types of fluid inclusion assemblages: 1) type A1a—large (> 100 µm) irregularly shaped fluid inclusions that occur in clusters; they also contain a solid phase and the volume fraction of the vapour phase varies between 10 and 30 vol%. 2) type A1b—trails of regularly- and negative-crystal shaped inclusions that are up to 20 µm in diameter and which volume fraction of the vapour phase varies between 40 vol% and 50 vol%. 3) type A1c—trails (healed cracks) of elongated to irregularly shaped fluid inclusions, locally all-liquid and up to 20 µm in length with the volume fraction of the vapour phase varying 5–10 vol%. The transitional zone contains many irregular, uniformly shaped fluid inclusions of type A1d; their sizes vary between 10 µm and 250 µm, whereas their relative abundances of vapour phase range 40–50 vol% and are similar to those shown by type A1b inclusion. The crystal rim has trails of type A1e fluid inclusions located along crystal growth zones; these fluid inclusions range in size 1–10 µm and their shapes are semi-regular, whereas the volume fraction of the vapour phase varies between 20 and 30 vol%.

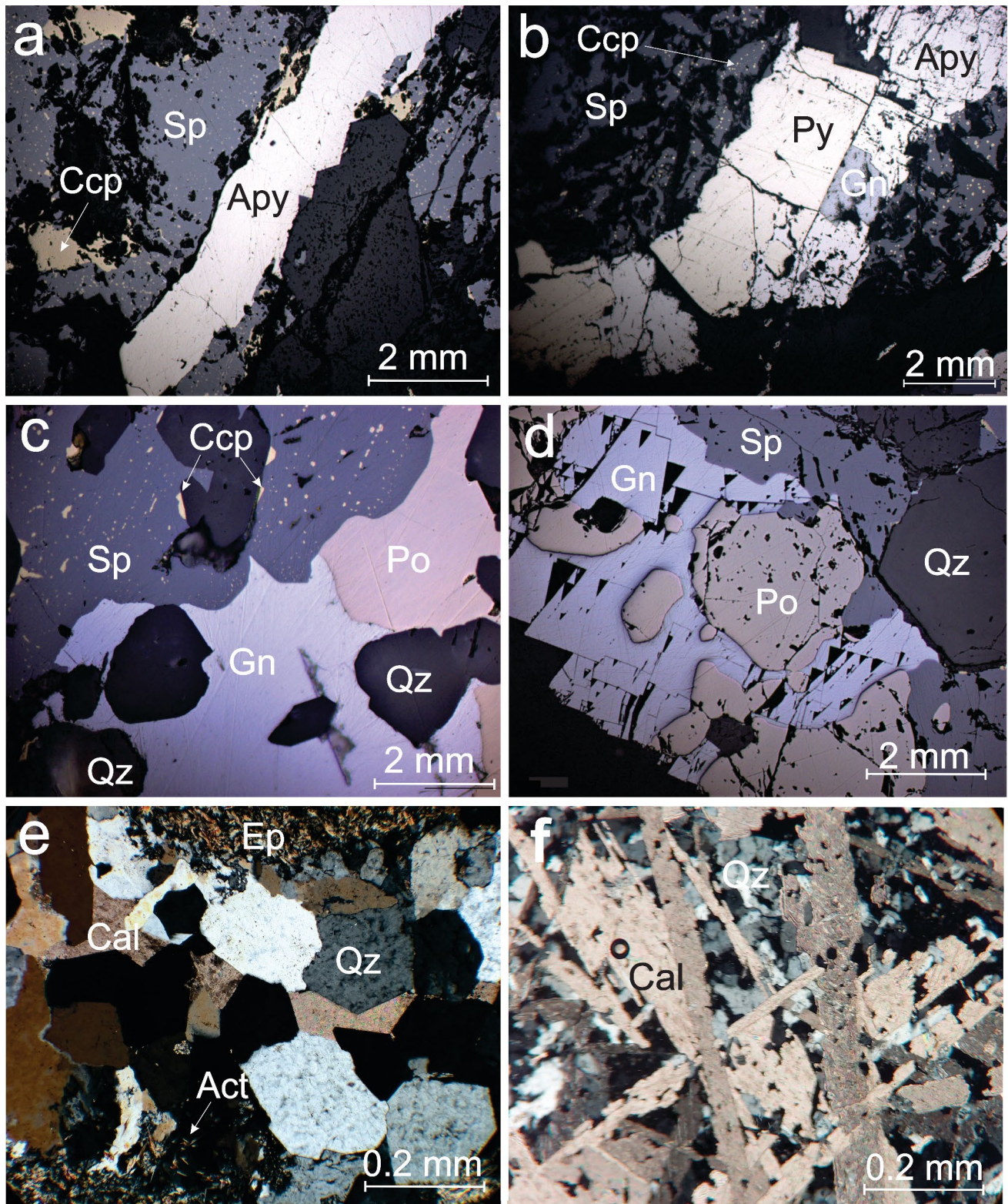


Fig. 4 Photomicrographs (a–d: reflected-light, e–f: transmitted-light) of ore-forming and rock-forming minerals from the Rudnik deposit. **a** Arsenopyrite vein cemented with sphalerite and chalcopyrite. **b** Arsenopyrite-pyrite vein cemented with sphalerite and galena. **c**, **d** Intergrowth of quartz and polymineral aggregate of pyrrothite, galena,

sphalerite, and chalcopyrite. **e** Quartz-calcite mosaically 'packed' vein in retrograde skarn. **f** Quartz-calcite intergrown. Abbreviations: Act-actinolite, Apy-arsenopyrite, Cal-calcite, Ccp-chalcopyrite, Ep-epidote, Gn-galena, Po-pyrrothite, Py-pyrite, Qz-quartz, Sp-sphalerite

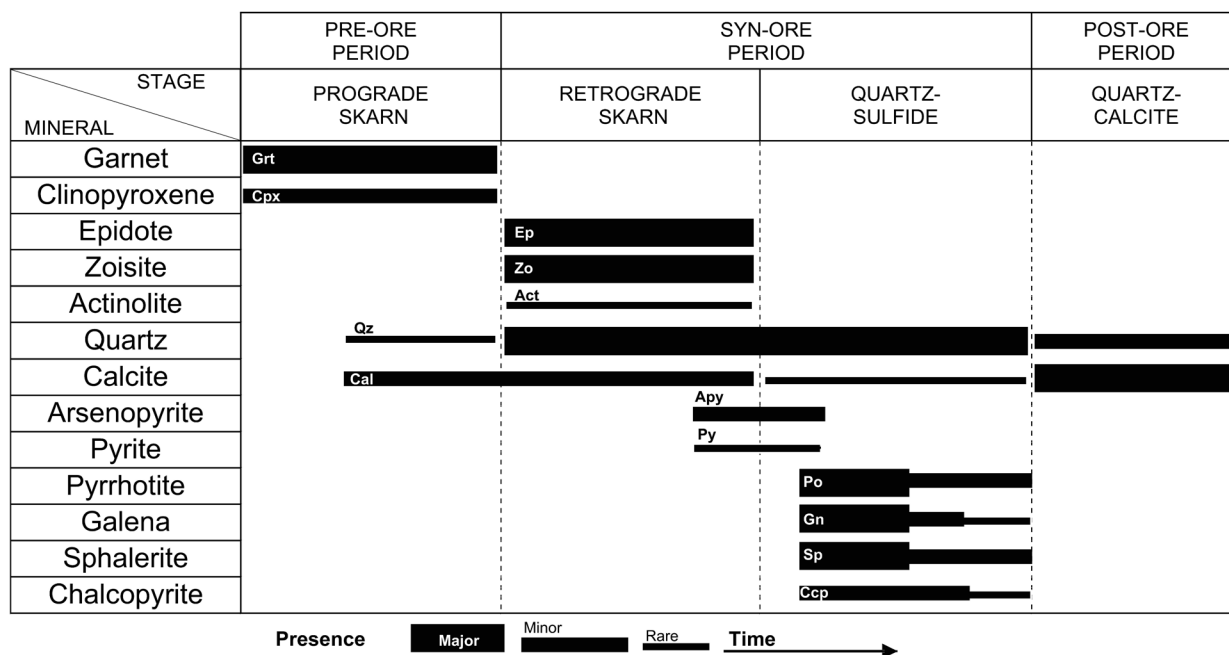


Fig. 5 Paragenetic sequences of the Rudnik deposit

In contrast to samples PR and A1, sample A2 hosts mainly healed fractures that crosscut grain boundaries without visible crystal growth zones (Fig. 7). We distinguish four types of fluid inclusions assemblages in this sample: 1) type A2a—fluid inclusions that appear in clusters; they are irregularly shaped and of variable size (10–50 μm); the liquid phase is more abundant than the vapour phase (20–30 vol%) and locally these inclusions may contain a solid phase as well. 2) type A2b—numerous regularly shaped fluid inclusions appearing in trails; they are 10–40 μm in length, while the volume fraction of the vapour phase varies between 30–40 vol. %; they may also contain a solid phase. 3) type A2c—vapour-rich fluid inclusions (vapour phase 80–90 vol%), regularly or negative crystal-shaped, and of small size (< 15 μm); these fluid inclusions occur together with type A2b in the same trails. 4) type A2d—liquid-rich to all-liquid fluid inclusions of irregular shape and size up to 10 μm in length; they occur in a few small clusters.

In sample AZ the zonal growth of quartz crystals is not visible, similarly to sample A2 (Fig. 7). We recognize three types of fluid inclusion assemblages: 1) type AZa—irregularly shaped fluid inclusions of different sizes (10–100 μm); they most often occur in clusters of several inclusions and subordinately as isolated inclusions; their volume fraction of the vapour phase varies 30–50 vol% and usually contain a solid phase; these inclusions are similar to those of type PRa and type A1a. 2) type AZb—numerous fluid inclusions that have regular and negative crystal shapes and are distributed along parallel trails; their size varies 10–40 μm , while the volume fraction of the vapour phase is most often ~ 50 vol%;

sometimes they contain visible solid phases. 3) Type AZc—negative-crystal- or regularly shaped fluid inclusions rich in the vapour phase (> 90 vol. %); these fluid inclusions are small (< 10 μm) and are located in trails. The petrographic singled-out fluid inclusion types and similarities in occurrences (see the preceding paragraphs) result in the definition of six groups within all samples: A, B, C, D, E, and F (Table 1).

Raman spectroscopy of fluid inclusions

Compositional fluid and gas properties determined by Raman spectroscopy strengthen the selected division of fluid inclusion types in groups A, B, C, D, E and F (Table 1, Fig. 8). A complete set of Raman spectra of individual inclusion types from each sample is provided in the Appendix 3, whereas representative spectra are shown in Fig. 8.

Group A is observed in all samples and is characterised by a relative high-salinity shape of the H_2O Raman spectrum of the liquid phase (Fig. 8a). At low temperatures, the frozen inclusions reveal the presence of mixtures of ice and hydrohalite spectra (Fig. 8b). The eutectic melting was detected between -25 and -20 $^\circ\text{C}$. These observations indicate that the liquid phase in the inclusions is mainly composed of a H_2O -NaCl mixture. The vapour phase consists of a gas mixture of up to 98 mol% CO_2 and a maximum of 7 mol% CH_4 (Fig. 8g). The relatively low intensity of the CO_2 and CH_4 Raman spectra implies a low density of the vapour phase.

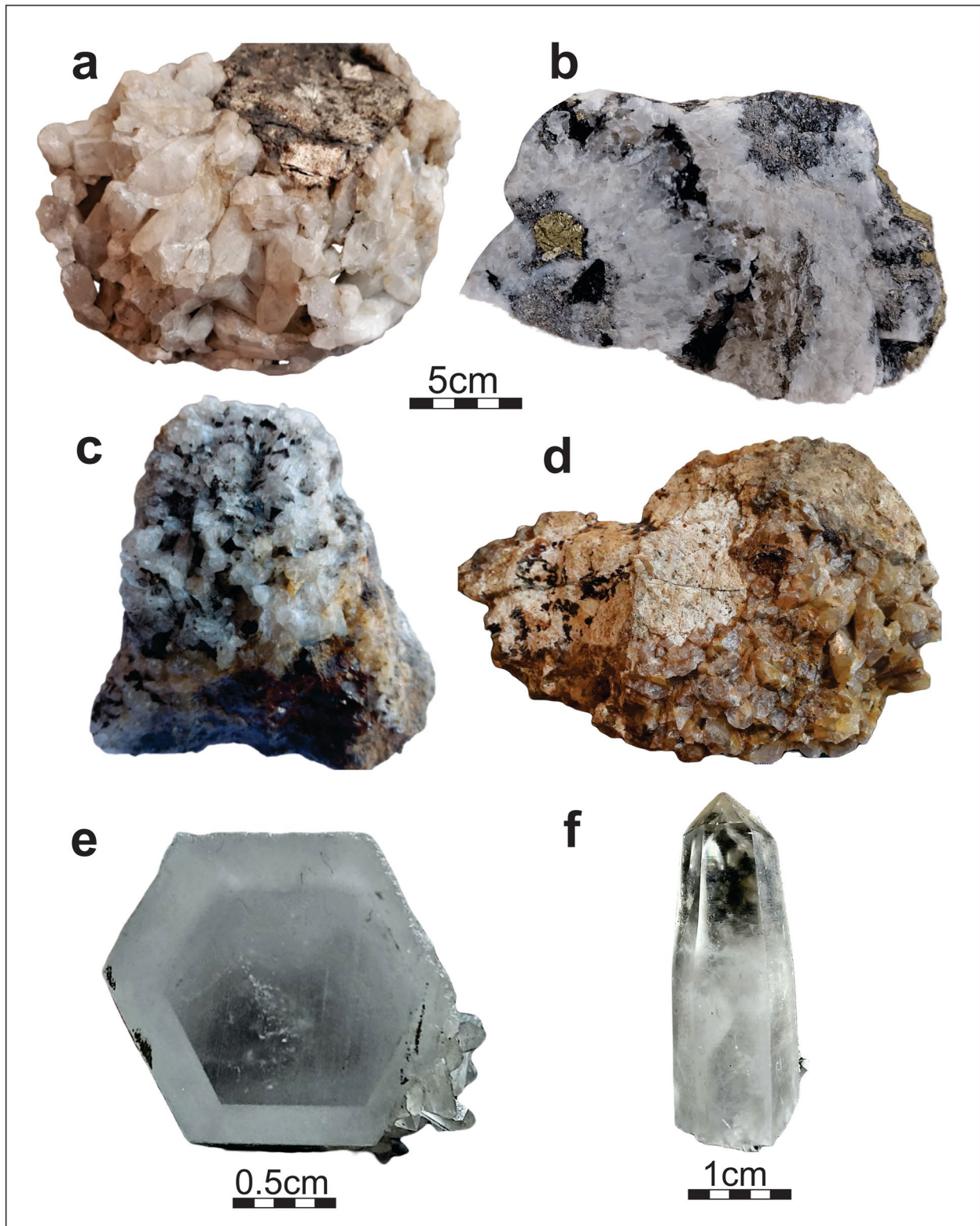


Fig. 6 Macroscopic images of quartz samples which fluid inclusions were studied. **a** Sample PR, quartz crystals from the Prljuša ore zone. **b** Sample A1, quartz with polymetallic mineralization from the Azna

ore body. **c** Sample A2, crystals between fragments of diatreme breccias. **d** Sample AZ, an aggregate of quartz crystals from the Z ore body. **e, f** Visible growth zones in a quartz crystal from sample PR

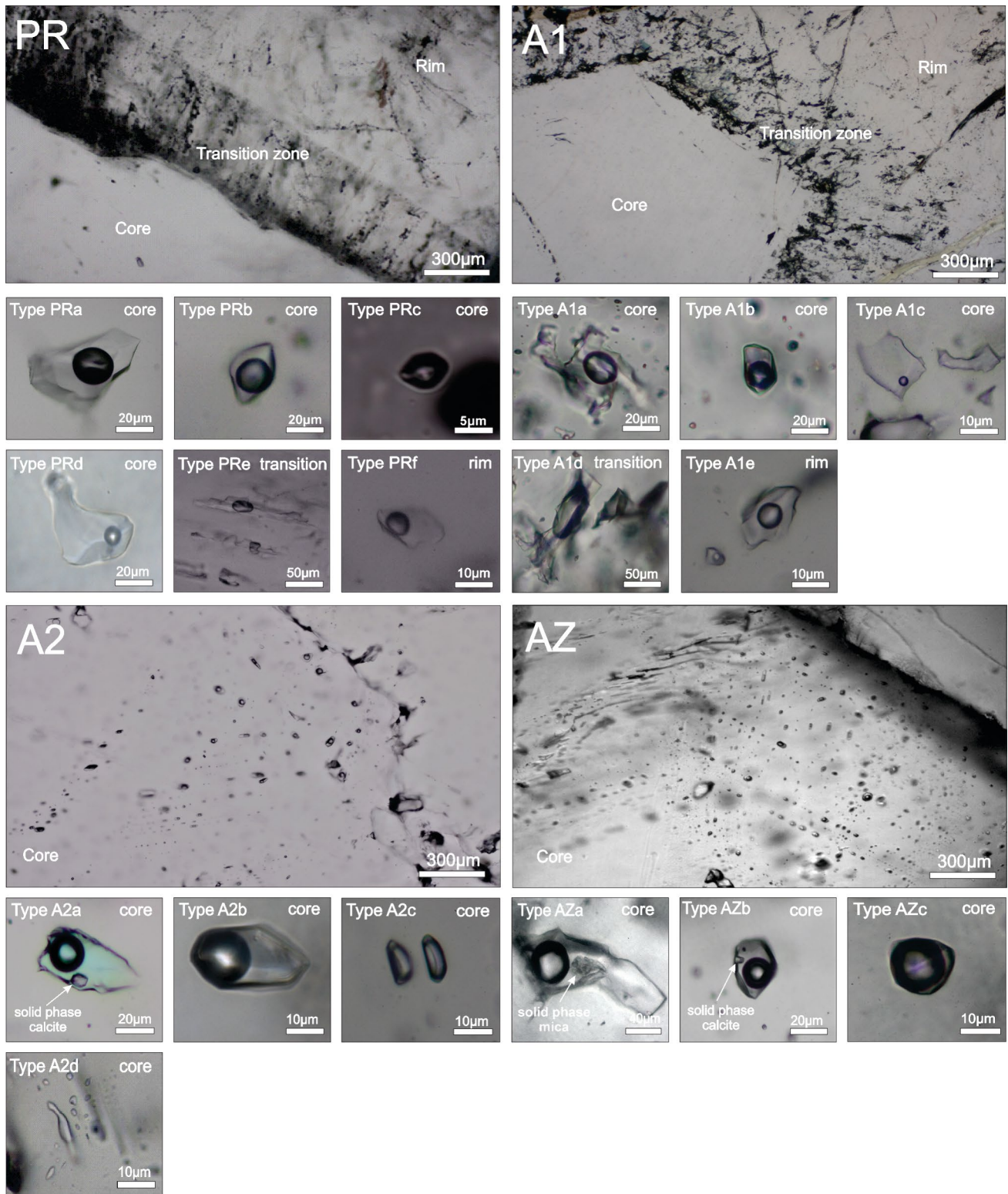


Fig. 7 Photomicrographs of different types of fluid inclusions from the studied samples PR, A1, A2 and AZ

The H_2O spectrum of Group B is significantly different from Group A (Fig. 8a), corresponding to a moderate salinity. The vapour phase is slightly enriched in CH_4 (up to 10 mol%)

compared to group A, but remains a CO_2 -rich gas mixture (Fig. 9c, g). Some inclusions (type PRb) reveal the presence of minor amounts of additional H_2S . Group A and B fluid

Table 1 Microthermometry and bulk properties of groups of fluid inclusions (A-F). Phase transitions: LV → L = two-phase inclusions with fluid and vapour (LV) transform to a one-phase liquid state (L); SLV → L = two-phase inclusions with ice and vapour (SLV) transform to a one-phase liquid state (L)

group	(n)	vapor fraction	T_h LV → L	T_m SLV → LV	salinity	molar volume	density	P_h
unit		vol%	°C	°C	wt%	L/mol	g/cm ³	MPa
A	78	20–30 (10–50)	380–390 (349–432)	-8 to -10 (-6 to -22.8)	12–16 (9–24)	25	0.81	15
B	82	50–60 (30–60)	370–380 (340–420)	-3 to -4 (-2.4 to -8.5)	6–7 (4–12)	26	0.76	15
C	4	90–100 (80–100)	-	(-1 to -4)	1–6	-	-	-
D	18	0 (0–10)	180–200 (148–245)	-2 to -3 (-0.7 to -4.9)	4–5 (1–8)	20	0.94	0.5
E	36	40–50 (10–50)	360–380 (235–401)	-3 to -3.5 (-1 to -6)	4–5 (2–8)	29	0.64	21
F	27	20–30 (20–30)	340–360 (259–365)	-2 to -3 (-1.8 to -4.7)	4–5 (2–5)	28	0.67	16

inclusions occasionally contain solid phases, i.e. accidentally trapped small crystals of calcite and mica (Fig. 8e, f).

The vapour-rich inclusions of group C contain a gas mixture of CO₂, CH₄ and H₂S (Fig. 8c, d). Sample AZ are enriched in CH₄ (up to 13 mol%) in addition to H₂S (up to 10 mol%), whereas samples PR and A2 reveal lower concentrations of CH₄ (up to 4 mol%) and H₂S (up to 6 mol%) compared to group B (Fig. 8g). The H₂O spectrum exhibits a relatively high shoulder at about 3200 cm⁻¹ that imply low salinity characteristics (Fig. 8a). CH₄ and H₂S dissolved in the liquid phase are also detected in Raman spectra (Fig. 8c).

Group D contains liquid-rich (vapour bubble volume fraction less than 5 vol%) to all-liquid fluid inclusions that reveal nearly pure H₂O Raman spectra.

Group E contains a vapour phase that is relatively enriched in CH₄ (up to 17 mol%), and up to 89 mol% CO₂ (Fig. 8g), whereas H₂S has not been detected. The relative intensity of the CH₄ and CO₂ Raman spectra implies higher densities than observed in the vapour phase of groups A, B and C. The Raman band of the liquid phase corresponds to a low salinity aqueous solution, similar to group C.

Group F inclusions are less enriched in CH₄ compared to group E given that maximally 13 mol% CH₄ is detected (Fig. 8g). The CO₂ contents may reach values of up to 95 mol%. The low intensity of these Raman bands implies again a very low density of the vapour phase. The Raman spectrum of the liquid phase resembles a low salinity aqueous solution.

Microthermometry and bulk properties calculations

Microthermometry analyses comprise a total population of 241 fluid inclusions: 81 from PR, 68 from A1, 48 from A2 and 44 from sample AZ. The method is used to determine the homogenization temperature (T_h), dissolution temperature of ice (T_m), the temperature of the first appearance of

liquid (T_c) and nucleation temperature (T_n) upon cooling experiments. Due to the low density of the gas mixture in the vapour phase and low concentrations of gases in the aqueous solution, calculations of bulk properties, such as density and composition can be performed in a simplified binary system of H₂O and NaCl. The main characteristics of the fluid inclusions groups (A, B, C, D, E and F) are summarized in Table 1, whereas all measured and calculated data are given in Appendix 4.

Group A

Homogenization temperatures display a normal distribution (Fig. 9, Table 1) with a mode at about 380 to 390 °C (average 388 °C), within a relatively small range of 349 to 432 °C. A slightly higher T_h is obtained in sample AZ (399 °C) and A2 (391 °C) compared to PR (377 °C) and A1 (379 °C). Dissolution of ice occurs between -8 and -10 °C (mode) with an asymmetric distribution in the range from -6 to -22.8 °C (Fig. 9, Table 1). These temperatures correspond to a calculated salinity mode ranging from 12 to 16 wt% NaCl (average of 15.3 wt% NaCl). Cryo-Raman spectroscopy shows the presence of NaCl as a major salt component of the aqueous liquid solution. The calculated density varies between 0.74 and 0.78 g/cm³ (mode), with an average value of 0.74 g/cm³. The pressure at homogenization is calculated at 15 MPa (mode).

Group B

Both T_h and T_m are represented by a normal distribution in a histogram (Fig. 9, Table 1), with a mode at 370 to 380 °C of T_h and -3 to -4 °C of T_m . The average T_h is 375 °C and measurements are within the range 340 to 420 °C without significant differences in T_h in all samples. The corresponding salinity is 6 to 7 wt% NaCl (mode) with an average value of 6.7 wt% NaCl.

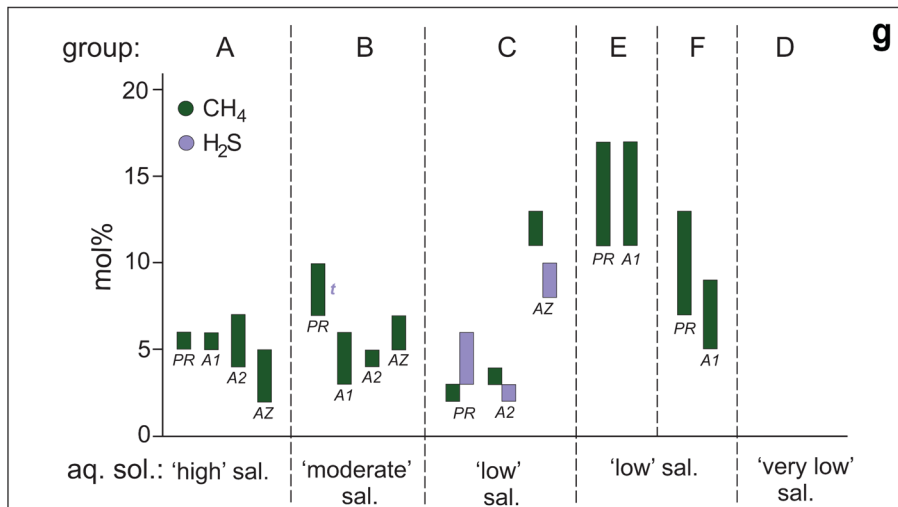
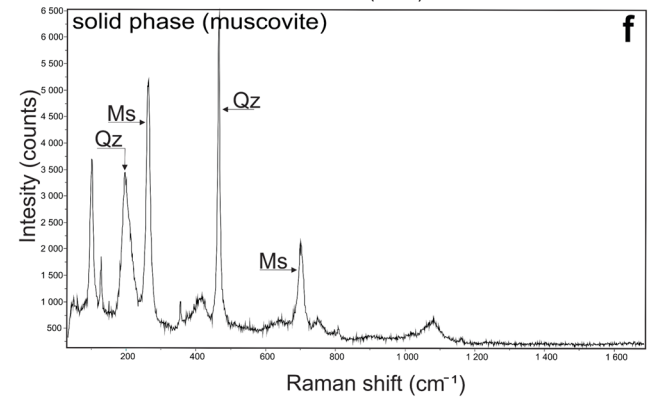
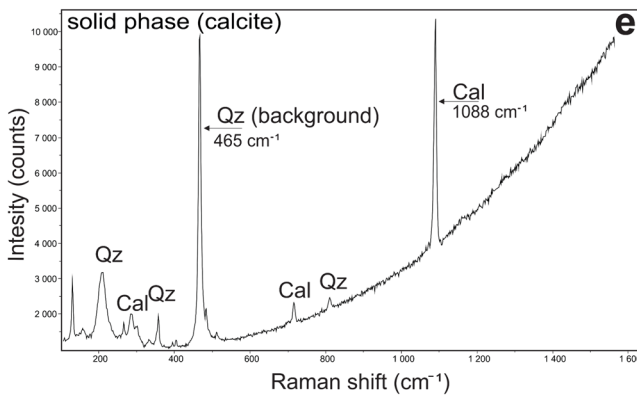
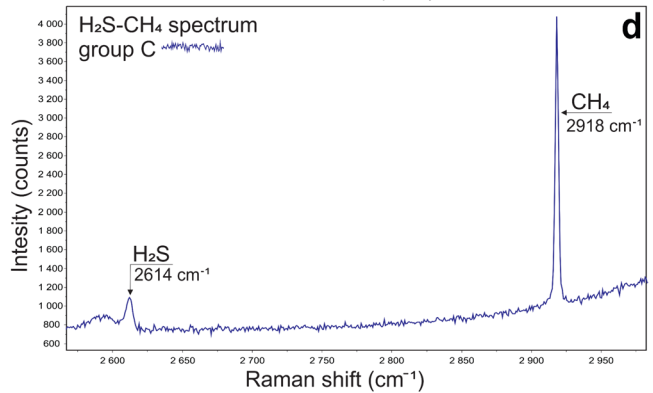
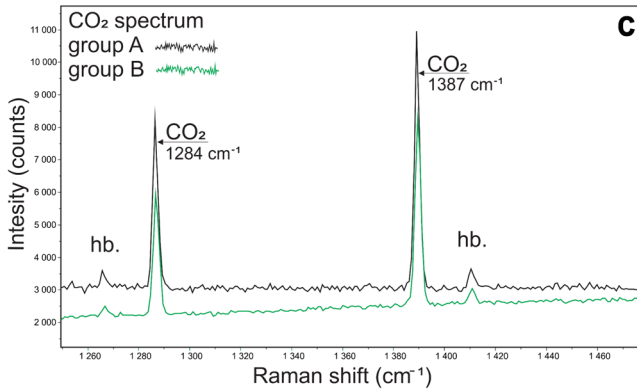
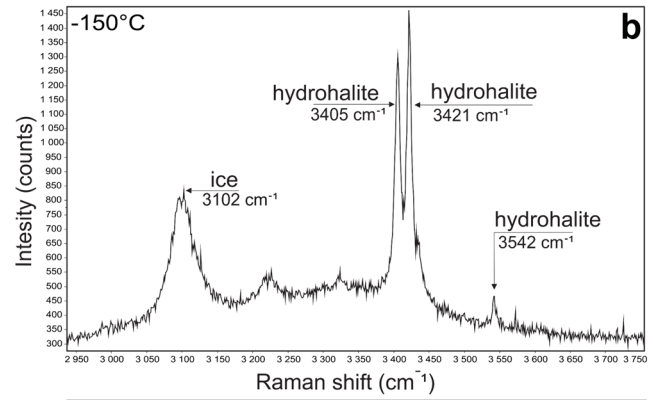
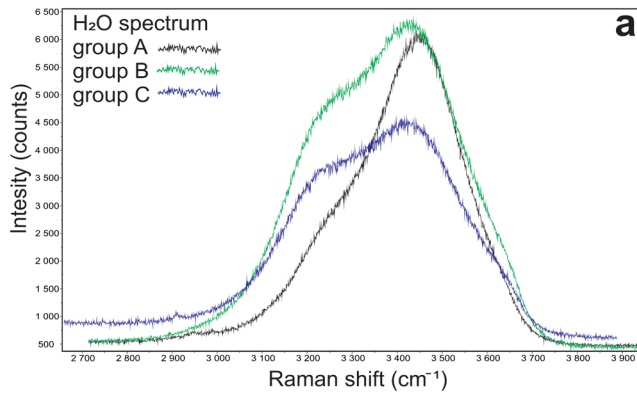


Fig. 8 a-f Representative Raman spectra. **a** Different salinities in a H₂O spectrum. **b** Raman spectrum of a frozen inclusion: ice and hydrohalite. **c** Examples of CO₂ spectra. **d** Examples of CH₄ and H₂S spectra. **e** Accidentally trapped calcite spectra. **f** Accidentally trapped muscovite spectra. Abbreviations: cal-calcite, ms-muscovite, qz-quartz. **g** CH₄ and H₂S content (in mol%) in vapour bubbles that are mainly composed of CO₂, based on Raman spectroscopic measurements; symbol *t* indicates the presence of traces of H₂S

The T_h values are slightly lower, and the salinity is significantly lower in group B inclusions than in those from group A. The density of the inclusions is calculated at 0.62 to 0.64 g/cm³ (mode), with an average value of 0.64 g/cm³. The pressure at homogenization is calculated at 15 MPa (mode).

Group C

The low density of the vapour phase does not allow any microthermometric analysis, i.e. homogenization or melting of CO₂ is not observed. Because of that, total homogenization in the vapour phase is determined only with insufficient accuracy. Locally, the final ice melting temperature of the frozen aqueous phase in these inclusions occurs at temperatures of -1.0 to -4.0 °C, corresponding to a salinity of 1 to 6 wt% NaCl.

Group D

This group contains many all-liquid inclusions and some with a small vapour bubble. Microthermometry could only be applied to the latter. The absence of a vapour bubble may represent a metastable state. Homogenization temperatures are significantly lower and occur in the range of 148 to 245 °C (average 179 °C). T_m occurs in the range from -0.7 to -4.9 °C and the corresponding low salinity varies between 1.2 and 7.7 wt% NaCl.

Group E

Inclusions in group E homogenize at a mode of 360 to 380 °C, in the range from 235 to 401 °C (Fig. 9, Table 1), at similar conditions compared to group B. In sample A1, homogenization temperatures are higher (375 °C) compared to sample PR (361 °C). Dissolution of ice occurs between -1 and -6 °C corresponding to a salinity of 2 to 8 wt% NaCl (Fig. 9, Table 1). Two outliers occur at lower T_h and T_m values and may represent mixing with group D fluids. The density is calculated at 0.60–0.65 g/cm³ (mode) and range from 0.57 to 0.83 g/cm³. The pressure at homogenization is calculated at 20 to 25 MPa (mode).

Group F

Inclusions in group F reveal homogenization at 340–360 °C (mode), in the range from 259 to 385 °C (Fig. 9, Table 1).

These temperatures are significantly lower than T_h in group E and higher than T_h in group D. The dissolution of ice occurs at a mode of -2 to -3 °C, corresponding to a salinity of 4–5 wt% NaCl. The corresponding densities are calculated at 0.65–0.70 g/cm³ (mode). In sample A1, the value of the homogenization temperature (349 °C) is slightly higher compared to sample PR (337 °C).

Discussion

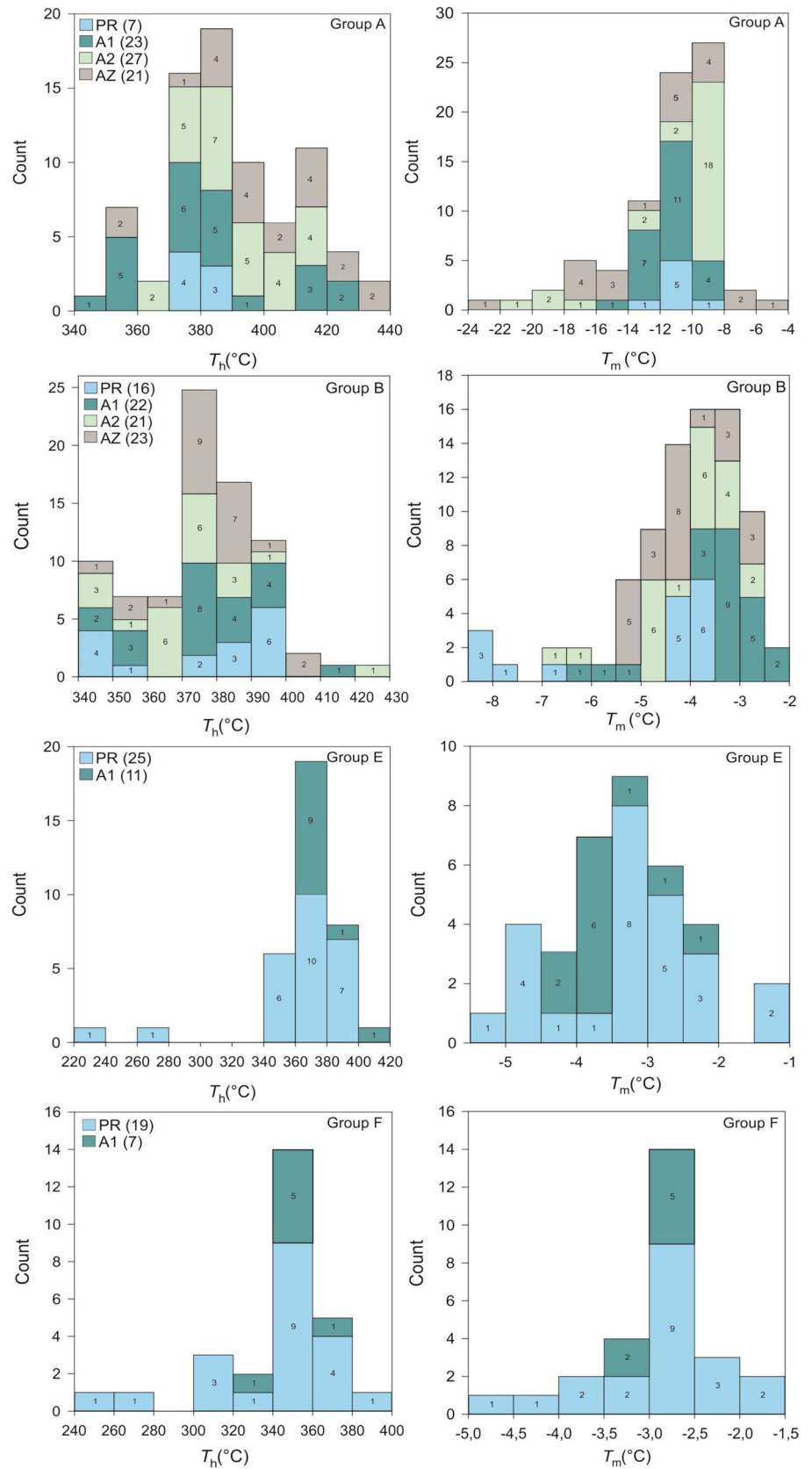
Fluid evolution trends

The above defined groups of quartz-hosted fluid inclusions are plotted in a combined T_h versus salinity diagram that illustrates the development of fluid properties from cores to rims (Fig. 10).

Dilution of the fluid at nearly constant high temperatures is reflected by the transition from relatively large inclusions in clusters (group A) to inclusions in trails within the crystal cores (group B). Cooling at nearly constant salinities is illustrated by the transition from fluids trapped in the first overgrowth zone (group E) to those in growth zones in the outer rims (group F). Group D inclusions, which appear both within rims and cores, are late, and possibly represent infiltration of meteoric solutions (nearly pure H₂O) along cracks.

The presence of liquid-rich (groups A and B) and vapour-rich inclusions (group C) in crystal cores suggests a boiling assemblage. The preservation of mainly liquid-rich inclusions, and the rare occurrence of vapour-rich inclusions is also in agreement with the hypothesis of a boiling event (e.g. Roedder 1984). Within a simple binary system of H₂O and NaCl, boiling produces low-density vapour-like and high-density liquid-like fluids that are relatively enriched in H₂O and NaCl, respectively (e.g. Bakker 2019). This distribution effect corresponds to the observation of salinities in group B and group C and corresponds to the volume fractions of vapour bubbles in both types of inclusions at room temperature. The most relevant consideration is the distribution of gases such as CO₂, CH₄, and H₂S between liquid-rich group B and vapour-rich group C inclusions. The distribution can be modelled with an equation of state that includes water, gas mixtures and salt. Only few of these equations are available (e.g. Bakker 1997). For example, a homogeneous H₂O-rich fluid (90 mol% H₂O, 4.5 mol% CO₂, 0.5 mol% CH₄, 5 mol% NaCl) may unmix at 350 °C and 62 MPa by producing vapour bubbles that are relatively enriched in gas-mixtures (CO₂-CH₄) and depleted in NaCl. On further cooling, the liquid phase will become enriched in NaCl and depleted in gas components, whereas the opposite occurs in the vapour phase. The relative proportions of CO₂ and CH₄ in the gas mixture evolve in distinct manners, as the vapour phase is relatively enriched in CH₄ and the

Fig. 9 Frequency distribution of homogenization temperature (T_h) and dissolution temperature of ice (T_m) in groups A, B, E and F



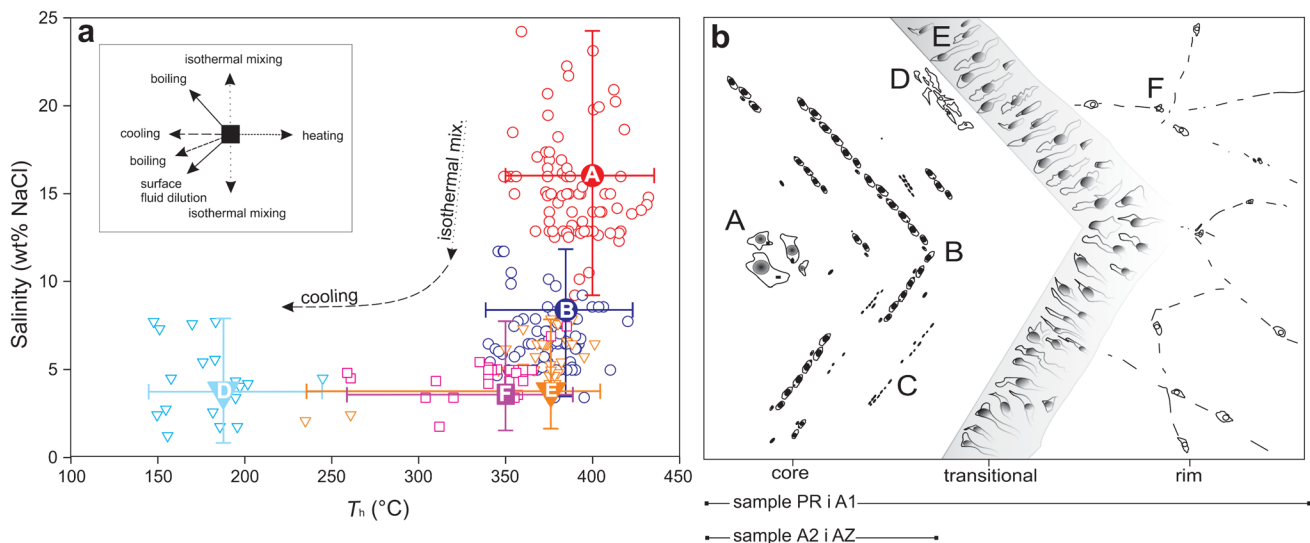


Fig. 10 **a** Variations of T_h and salinity for the studied samples of the Rudnik ore deposit (trends of fluid evolution according to Wilkinson 2001). **b** Mode of occurrence and textural relationships between the groups of fluid inclusions in the examined samples

liquid phase is relatively enriched in CO_2 . H_2S is assumed to behave similarly as CH_4 during boiling. These considerations are inconsistent with the observation that group C inclusions have lower concentrations of CH_4 than group B inclusions (Fig. 8g).

The original fluid composition is potentially represented by group A inclusions that contain mainly a H_2O -NaCl mixture with minor amounts of CO_2 and traces of CH_4 . Group B inclusions record a dilution of the original fluid at nearly constant temperatures, with a slight increase in CH_4 contents. Subsequently, the system was infiltrated by a fluid phase that is rich in volatiles, mainly CO_2 with significant amounts of CH_4 and H_2S (group C fluids). This volatile-rich fluid must have originated in similar depths evolving by phase separation of another type of supercritical fluid.

A subsequent stage of fluid entrapment is illustrated in rim areas of single quartz crystals (Fig. 10): a H_2O -rich fluid with significant amounts of CO_2 and CH_4 and the absence of H_2S (group E). The abrupt change in the fluid regime is visualized by the occurrence of overgrowth textures, whereas the temperature is similar to those obtained for group B (Fig. 10).

The transition of group E to F may represent a boiling effect upon cooling of the system with group F representing the residual liquid in a relatively low salinity system. The produced vapour phase is lost in an open pore system, consequently, the gas mixture in the remaining liquid phase is relatively enriched in CO_2 (Fig. 8g: lower CH_4 in group F). Finally, a late-stage fluid is represented by group D that corresponds to a trapping event at relatively low temperatures.

Constraints on the skarn and ore formation

Pressure and temperature conditions of skarn and ore formation are determined from isochores of the fluid inclusion groups and mineral paragenesis in the skarn. Isochores are calculated from microthermometric data for mode values of fluid inclusion groups A, B, E, and F. Group D is associated with processes of post-ore formation (mixing with meteoric fluids, quartz-calcite stage) and group C (low density of the vapour phase) is not considered in the calculation.

Figure 11a shows that all fluid inclusions were trapped within a relatively similar P-T range. The calculated isochores for groups A, B, E, and F correspond to shallow contact metamorphic conditions (i.e. albite-epidote and hornblende-hornfels facies conditions). We can assume that the lower limit of the skarn formation is the minimum temperature at which epidote is formed (~ 250 °C), whereas the upper limit is marked by the presence of grossular-andradite in a temperature range between 400 and 700 °C. In the presence of quartz, grossular is stable up to ~ 600 °C, when these two minerals react to form wollastonite and anorthite (e.g. Storre 1970). The absence of wollastonite and plagioclase (anorthite) in these skarns indicates maximum formation temperatures of ~ 600 °C.

In addition, homogenization temperatures determined by fluid inclusions with boiling features (groups E and F) represent absolute fluid trapping temperatures and may strengthen the above conclusions (Roedder 1984). Boiling groups are also important in the assessment of trapping pressures of fluid inclusions. We estimate trapping pressure

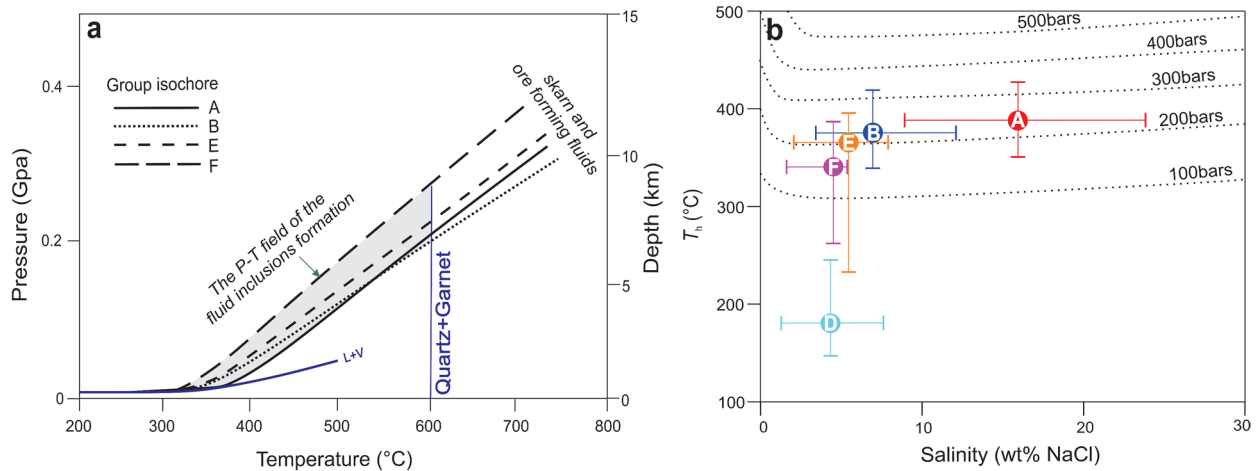


Fig. 11 **a** Pressure and temperature conditions of skarn and ore formation determined from calculated isochores of the fluid inclusion groups and mineral paragenesis in the skarn. The P–T field of the for-

mation of the studied fluid inclusions is highlighted in gray. **b** Pressure values calculated for the studied fluid inclusion groups in the NaCl–H₂O system after Driesner and Heinrich (2007)

applying the isobaric equations of Driesner and Heinrich (2007) using the software AqSo_NaCl (Bakker 2018, 2019) and the defined boiling groups. The estimate entrapment pressures for groups E and F range from 180 to 220 bar (mode) (Fig. 11b). We consider that trapping pressure in a boiling fluid system is equal to hydrostatic pressure (e.g. Roedder and Bodnar 1980; Zhong et al. 2014; Zhou et al. 2017). Based on this conclusion, the homogenization of liquid-rich inclusions can be taken as trapping conditions, using the important assumption that coexisting vapour-rich fluids are not trapped. We infer that the pressure range for all groups of 180 to 330 bar corresponds to the boiling of hydrothermal fluids at a depth of ~2 km under hydrostatic pressure conditions.

Similarities with fluid properties in Zn-Pb skarn deposits

The Zn-Pb skarn deposits form by slightly saline and lower temperatures fluids compared to other types of skarn deposits; in addition, the most abundant volatile component of these fluids is CO₂, whereas CH₄ is present in minor amounts (e.g. Baker et al. 2004; Meinert et al. 2005; Canet et al. 2011; Bodnar et al. 2014; Jimenez-Franco et al. 2020; Sun et al. 2021; Zhao et al. 2021). Processes such as "boiling" and "mixing" of fluids at similar conditions are noted as important for the formation of these deposits; this usually involves three separated periods: pre-ore, syn-ore, and post-ore period (e.g. Kwak 1986; Baker and Lang 2003; Shu et al. 2017; Guo et al. 2021), although some of these periods are absent in certain cases (e.g. Canet et al. 2011).

The present work on fluid inclusions within quartz crystals from the Rudnik deposit allows for recognizing the effects of the above mentioned periods. The role of relatively high temperature- (> 400 °C) and high-salinity fluids (35–50 wt% NaCl), i.e. halite bearing fluid inclusions in the pre-ore period is not observed, although mineral paragenesis of this high-grade skarn period is indeed recognized. On the other hand, evidence for the latter two periods is documented. During the syn-ore period hydrous minerals such as epidote, coisite, and actinolite form, under the influence of fluids characterized by lower temperatures (< 400 °C) and lower salinity of < 25 wt% NaCl; this is accompanied by the activation of fluids of similar properties and the precipitation of sphalerite, galena, and chalcopyrite (the main ore stage). The post-ore period marks nearly pure H₂O at temperatures below 200 °C. The T_h -salinity pairs in the studied system are similar to the values of other Zn-Pb skarns, supported by a relatively low T_h ranging 150–420 °C, salinity up to 25 wt% NaCl and the lack of correlation between T_h and salinity, as is reported for this type of skarn deposits (Bodnar et al. 2014). CO₂ is the most abundant volatile component in all fluid inclusion groups, with minor amounts of CH₄, indicating relatively oxidized skarn systems that develop at shallow depths and in distal geological settings of the associated magmatic intrusion. Processes such as "boiling" and "mixing" of fluids at similar conditions are deciphered in the present work, illustrating that melting temperatures and vapour component analyses are the most convenient parameters to determine the boiling process, whereas the measurement of total homogenization in the vapour phase may include large uncertainties and are often not feasible.

Implications for the genesis of the Rudnik deposit

Figure 12 shows a simplified four step model of the formation of the Rudnik deposit as the result of the activation of a hydrothermal system in the proximity to a Miocene magmatic intrusion. The model summarizes the results of this study and outlines the evolution of fluid properties through different stages of the deposit formation.

The intrusion of a magmatic body resulted in prograde anhydrous contact metamorphism observed only locally in the deeper parts of the deposit; this subsequently weakened the surrounding rocks allowing the injection of apical quartz-latitude dykes (Fig. 12a), as observed in many similar systems worldwide (e.g. Burnham 1979; Yang and Bodnar 1994; Fournier 1999; Meinert et al. 2003).

The injection of apical quartz-latitude dykes induced a slow ascent of hydrothermal fluids that have accumulated above the inferred magmatic intrusion. The thermal mass

of uncooled quartz-latitude dykes allowed gradual cooling, which controlled the spatial evolution of fluids away from the magmatic intrusion without the fluid boiling process. These fluids, with a salinity of up to 25 wt% NaCl and incidentally trapped calcite and muscovite crystals (groups A and B), resulted in widespread retrograde hydrous alteration of skarns in the deposit at temperatures ~350–400 °C (Fig. 12b). The composition of gas mixtures including their CO₂/CH₄ ratios in these inclusion groups reveals a higher oxidation state in the hydrothermal fluids that limited the sulfur activity; hence, sulfides did not considerably precipitate during this retrograde skarn stage, which is also recognized in the mineral paragenesis formed during this period. Subsequent enrichments in highly acidic volatiles (group C) resulted in intensive alteration of country rocks above the magmatic intrusion, leading to a progressive increase of permeability and gradual descending of meteoric water (Fig. 12c). Accumulation of gases and introduction

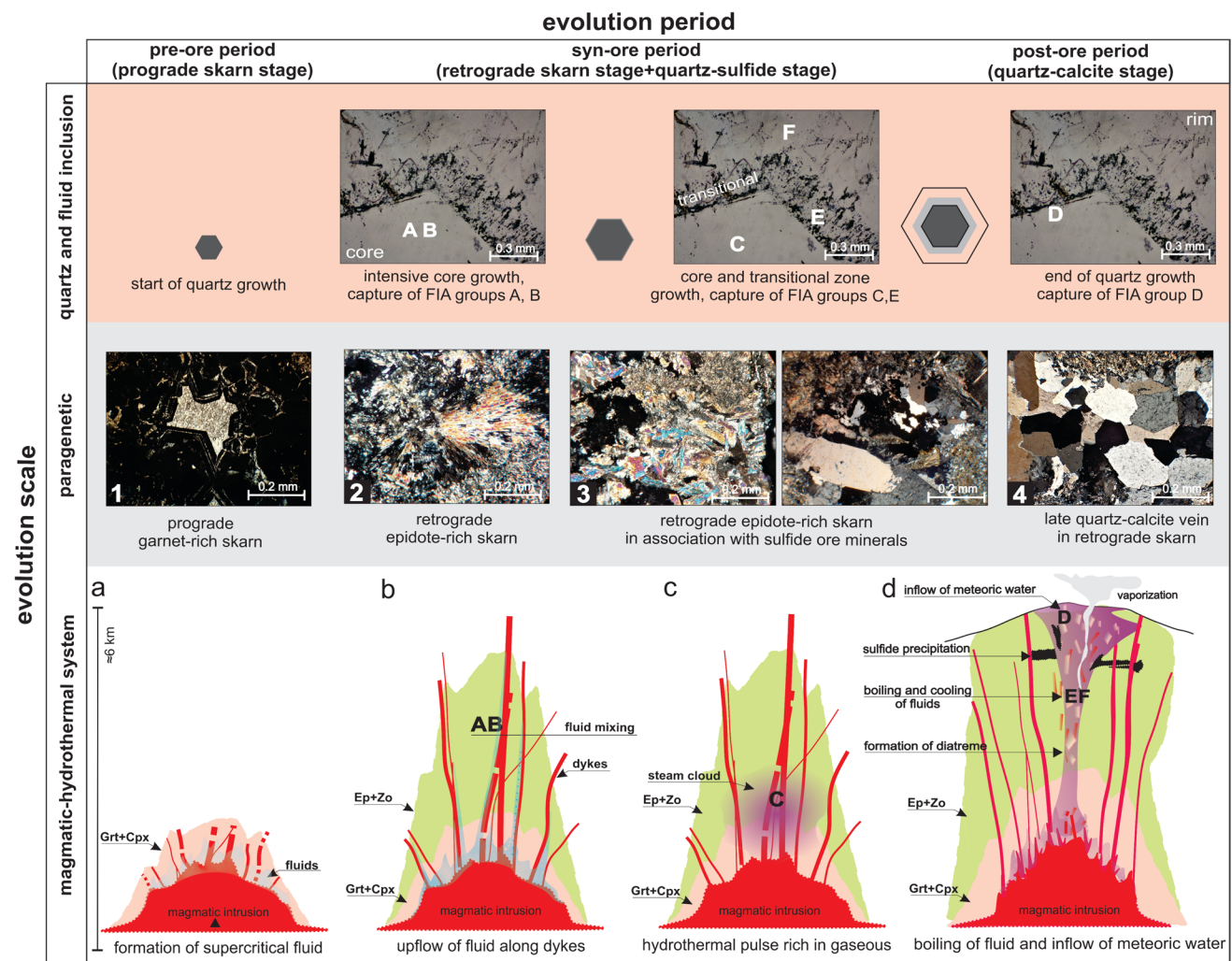


Fig. 12 A simplified model of hydrothermal fluids evolution and their role in the formation of the Rudnik skarn deposit (see text for explanation)

of meteoric water into the hydrothermal system increased pressure and resulted in phreatomagmatic fragmentation and formation of diatreme breccias. These explosive events led to pressure changes, boiling and incipient cooling of the hydrothermal system, which is evident in differences in P–T values calculated for fluid inclusions found in transitional and rim zones of quartz crystals (groups E and F, Table 1). The exceptionally high CH₄ content in these groups marks the onset of intensive percolations of meteoric water through diatreme channels and extraction of significant amounts of CH₄ from the wall rocks under reducing conditions. These events led to a decrease in temperatures and oxygen fugacity of fluids and established the conditions for ore precipitation. Additional release of acid volatiles from fluids (CO₂, H₂S) and reactions between sulfur species (H₂S, HS⁻) led to an increase in pH state. This caused the instability of metal complexes in an ore-forming fluid and deposition of Zn, Pb, Cu, and Ag in the quartz-sulfide stage, as reported from other skarn systems (e.g. Heinrich 2007; Zhang and Audétat 2018; Shu et al. 2021; Zhao et al. 2021; Fig. 12d). The activation of an almost pure H₂O fluid, often without CO₂, which is inferred from the presence of fluid-rich fluid inclusions (group D), characterizes the final, quartz-calcite stage of the Rudnik hydrothermal system. Significantly reduced *T_h* and very low salinity indicate fluid flow in a cooled magmatic-hydrothermal system (<245 °C) during the post ore processes.

Conclusions

We studied fluid inclusion assemblages hosted in sulfide-accompanied hydrothermal quartz in order to track the physicochemical evolution of hydrothermal fluids that precipitated the polymetallic Zn-Pb-Cu-Ag ore in the Rudnik skarn ore deposit. The Rudnik hydrothermal system shows a general fluid evolution trend from high temperature/medium salinity to low temperature/low salinity conditions; fluid evolution in Rudnik is interpreted by mixing of fluids of different salinities at constant high temperatures (between groups A and B), introduction of fluids with high volatile contents (group C), cooling of fluids with constant salinity (between groups E and F), and the inflow of meteoric water (group D). Early fluids found in quartz cores (groups A and B) correspond to the stage of retrograde skarn alteration in the deposit, whereas the properties of fluid inclusions in quartz overgrowths (groups E and F) reflect the main stage of ore formation. The main trigger for the precipitation of metals (Zn, Pb, Cu and Ag) is cooling associated with phreatomagmatic brecciation and diatreme formation. This event is manifested in the appearance of overgrown quartz textures, homogenization temperatures, and the composition of gas mixtures of the fluid inclusions within the

overgrown zones. Fluid inclusion trends and the predominance of hydrous epidote-zoisite skarns containing sulfide minerals, as well as the spatial and temporal relationship between the host rocks and ore, all suggest that Rudnik corresponds to a distal Zn-Pb skarn deposit formed by significant transportation of hydrothermal fluids from a magmatic intrusion upwards.

Supplementary Information The online version contains supplementary material available at <https://doi.org/10.1007/s00710-024-00860-7>.

Acknowledgements This study is supported by the CEEPUS network: CIII-RS-0038: "EURO Geo-Sci" and by the scientific project funded by the Serbian Ministry of Education, Science and Technological Development No 176016. Vladica Cvetković thanks the Serbian Academy of Sciences and Arts, Projects F9 and F17. Authors thank to Company Rudnik and flotation Rudnik doo for the sampling permit and helpful internal documentation material for the study. We sincerely thank Mr Goran Umeljić for his help during field work. Careful and encouraging reviews by Federico Lucci and Martina Zucchi and editorial handling of Maarten Broekmans have been very helpful and are gratefully acknowledged.

Author contributions S.P. performed sampling, preparation of thick-sections and worked on the text of all chapters. Prepared all the figures. R.B. participated with S.P. in writing the fluid inclusions study results and discussion. V.C. and R.J. contributed to the writing of the Geological Setting and Geology of the Rudnik deposit chapters, as well as the conclusion. All authors reviewed the manuscript and agreed with the proposed text.

Data availability All data presented in the paper are available in the Electronic Supplementary Materials.

References

- Ahmed Z, Hariri MM (2006) Formation and mineral chemistry of a calcic skarn from Al-Madhiq. SW Saudi Arabia *Geochemistry* 66(3):187–201
- Atkinson WW, Einaudi MT (1978) Skarn formation and mineralization in the contact aureole at Carr Fork, Bingham, Utah. *Econ Geol* 73(7):1326–1365
- Baker T, Lang JR (2003) Reconciling fluid inclusion types, fluid processes, and fluid sources in skarns: an example from the Bismark Deposit, Mexico. *Miner Depos* 38:474–495
- Baker T, Van Achterberg E, Ryan CG, Lang JR (2004) Composition and evolution of ore fluids in a magmatic-hydrothermal skarn deposit. *Geology* 32(2):117–120
- Bakker RJ (1997) Clathrates: Computer programs to calculate fluid inclusion VX properties using clathrate melting temperatures. *Comput Geosci* 23(1):1–18
- Bakker RJ (2004) Raman spectra of fluid and crystal mixtures in the systems H₂O, H₂O–NaCl and H₂O–MgCl₂ at low temperatures: applications to fluid-inclusion research. *Can Mineral* 42(5):1283–1314
- Bakker RJ (2012) Thermodynamic properties and applications of modified van-der-Waals equations of state. In: Morales-Rodriguez R, ed. *Thermodynamics-Fundamentals and its Application in Science*. New York: Cambridge University Press 163–190. <https://doi.org/10.5772/50315>
- Bakker RJ (2018) AqSo_NaCl: Computer program to calculate p-T-V-x properties in the H₂O–NaCl fluid system applied to

- fluid inclusion research and pore fluid calculation. *Comput Geosci* 115:122–133. (Application AqSo_NaCl downloadable from <https://rohmin.unileoben.ac.at/downloads>; accessed [20.01.2024])
- Bakker RJ (2019) Package fluids. Part 5: The NaCl-H₂O system in fluid inclusion research and applications of the software AqSo_NaCl (Bakker, 2018). *Chem Geol* 525:400–413
- Baumgartner M, Bakker RJ (2010) Raman spectra of ice and salt hydrates in synthetic fluid inclusions. *Chem Geol* 275:58–66
- Blečić N (1974) Fluid inclusions and their application in the exploration of certain Yugoslav deposits of mineral raw materials. [Original title: Tečno-gasne inkluzije i njihova primena pri istraživanju pojedinih jugoslovenskih ležišta mineralnih sirovina.] Unpublished Master's Thesis, University of Belgrade, Faculty of Mining and Geology, Belgrade, Serbia
- Bodnar RJ, Lecumberri-Sanchez P, Moncada D, Steele-MacInnis M (2014) Fluid inclusions in hydrothermal ore deposits. *Treatise Geochem* 13:119–142
- Burnham CW (1979) Magmas and hydrothermal fluids. In: Barnes HL (ed) *Geochemistry of Hydrothermal Ore Deposits*, 2nd edn. John Wiley and Sons, New York, pp 71–136
- Calagari AA, Hosseinzadeh G (2006) The mineralogy of copper-bearing skarn to the east of the Sungun-Chay river, East-Azarbaidjan. *Iran J Asian Earth Sci* 28:423–438
- Canet C, González-Partida E, Camprubí A, Castro-Mora J, Romero FM, Prol-Ledesma RM, Sánchez-Vargas LI (2011) The Zn–Pb–Ag skarns of Zacatepec, Northeastern Oaxaca, Mexico: A study of mineral assemblages and ore-forming fluids. *Ore Geol Rev* 39(4):277–290. <https://doi.org/10.1016/j.oregeorev.2011.03.007>
- Chang Z, Shu Q, Meinert LD (2019) Skarn deposits of China. *Soc Econ Geol Spec Publ* 22:189–234
- Cvetković V, Šarić K, Pécsey Z, Gerdes A (2016a) The Rudnik Mts. volcano-intrusive complex (central Serbia): An example of how magmatism controls metallogeny. *Geol Croatica* 69(1):89–99
- Cvetković V, Prelević D, Schmid S (2016b) Geology of south-eastern Europe. In: Papić P, ed. *Mineral and thermal waters of south-eastern Europe*. *Env Earth Sci Springer International Publishing*, Switzerland 1–29. https://doi.org/10.1007/978-3-319-25379-4_1
- Dimitrijević MD (2000) Geological Atlas of Serbia No-14. Metallogenic map and map of ore formations. Ministry of Mining and Energy, Republic of Serbia
- Djoković I (2013) Report of structural and geological features of the Rudnik deposit [Original title: Izveštaj o strukturno-geološkim karakteristikama ležišta Rudnik.]. Fund of internal documents of the Rudnik mine company, Rudnik, Serbia
- Driesner T, Heinrich CA (2007) The system H₂O–NaCl. Part I: Correlation formulae for phase relations in temperature–pressure–composition space from 0 to 1000 C, 0 to 5000 bar, and 0 to 1XNaCl. *Geochim Cosmochim Acta* 71(20):4880–4901
- Einaudi MT, Meinert LD, Newberry RJ (1981) Skarn deposits. In: Skinner BJ (ed) *Econ Geol 75th Anniv Vol* 317–391. <https://doi.org/10.5382/AV75.11>
- Filipović I, Marković B, Pavlović Z, Rodin V, Marković O (1978) Basic Geological Map of SFRY 1:100000, Geology of the Gornji Milanovac sheet [Original title: Osnovna geološka karta SFRJ 1:100000. Tumač za list Gornji Milanovac L34–137]. Savezni geološki zavod, Beograd, Serbia
- Fournier RO (1999) Hydrothermal processes related to movement of fluid from plastic into brittle rock in the magmatic-epithermal environment. *Econ Geol* 94(8):1193–1211
- Gallhofer D, Quadt AV, Peytcheva I, Schmid SM, Heinrich CA (2015) Tectonic, magmatic, and metallogenic evolution of the Late Cretaceous arc in the Carpathian-Balkan orogen. *Tectonics* 34(9):1813–1836
- Guo XG, Gao JJ, Zhang DH, Li JW, Xiang AP, Li CJ, Wang SY, Jiao TL, Ren CH (2021) Genesis of the Erdaohe skarn Pb–Zn–Ag deposit in the Great Hinggan Range, NE China: evidence from geology, fluid inclusions, and H–O–S isotope systematics. *Ore Geol Rev* 140(104414):20
- Heinrich CA (2007) Fluid-fluid interactions in magmatic-hydrothermal ore formation. *Rev Mineral Geochem* 65(1):363–387
- Heinrich CA, Neubauer F (2002) Cu–Au–Pb–Zn–Ag metallogeny of the Alpine–Balkan–Carpathian–Dinaride geodynamic province. *Miner Depos* 37(6–7):533–540
- Hoerler J, Von Quadt A, Burkhard R, Peytcheva I, Cvetković V, Baker T (2022) The Karavansalija Mineralized Center at the Rogozna Mountains in SW Serbia: Magma Evolution and Time Relationship of Intrusive Events and Skarn Au±Cu–Pb–Zn Mineralization. *Front Earth Sci* 9:798701
- Janković S (1990) The ore deposits of Serbia: Regional metallogenic settings, environments of deposition, and types. [Original title: Rudna ležišta Srbije: regionalni metalogenetski položaj, sredine stvaranja i tipovi ležišta.] University of Belgrade, Faculty of Mining and Geology, Belgrade, Serbia
- Jelenković R (2014) A brief overview of the metallic mineral resources of Serbia. *European Geologist* 37:34–38
- Jelenković R, Kostić A, Životić D, Ercegovac M (2008) Mineral resources of Serbia. *Geol Carpath* 59(4):345–361
- Jimenez-Franco A, Canet C, Alfonso P, Gonzalez-Partida E, Rajabi A, Escalante E (2020) The Velardeña Zn–(Pb–Cu) skarn-epithermal deposits, Central-Northern Mexico: new physical constraints on ore-forming processes. *Bolotín De La Sociedad Geologica Mexicana* 72:A270719
- Kostić B, Srećković-Batočanin D, Filipov P, Tančić P, Sokol K (2021) Anisotropic grossular-andradite garnets: Evidence of two stage skarn evolution from Rudnik, Central Serbia. *Geol Carpath* 72(1):17–25
- Kwak TAP (1986) Fluid inclusions in skarns (carbonate replacement deposits). *J Metamorph Geol* 4(4):363–384
- Lattanzi P (1991) Applications of fluid inclusions in the study and exploration of mineral deposits. *Eur J Mineral* 3(4):689–702
- Lu HZ, Liu Y, Wang C, Xu Y, Li H (2003) Mineralization and fluid inclusion study of the Shizhuyuan W–Sn–Bi–Mo–F skarn deposit, Hunan Province. *China Econ Geol* 98(5):955–974
- Meinert LD, Dipple GM, Nicolescu S (2005) World Skarn deposits. In: Hedenquist JW, Thompson JFH, Goldfarb RJ, Richards JP, ed. 100th anniversary volume. *Soc Econ Geol* 299–336. <https://doi.org/10.5382/AV100.11>
- Meinert LD, Hedenquist JW, Satoh H, Matsuhisa Y (2003) Formation of anhydrous and hydrous skarn in Cu–Au ore deposits by magmatic fluids. *Econ Geol* 98(1):147–156
- Melcher F, Reichl C (2016) Economic Geology of the Eastern and South-eastern European (ESEE) Region. *Berg Huettenmaenn Monatsh* 162:238–244. <https://doi.org/10.1007/s00501-017-0625-4>
- Milovanović D (2009) Petrological examinations of volcanic and metamorphic rocks of the Rudnik mine-in Serbian [Original title: Petrološka ispitivanja vulkanskih i metamorfih stena rudnika Rudnik], Fund of internal documents of the Rudnik mine company, Rudnik
- Palinkaš SS, Palinkaš LA, Renac C, Spangenberg JE, Lüders V, Molnar F, Maliqi G (2013) Metallogenic model of the Trepča Pb–Zn–Ag skarn deposit, Kosovo: evidence from fluid inclusions, rare earth elements, and stable isotope data. *Econ Geol* 108(1):135–162
- Petrović S, Batočanin N (2019) The alteration style in peridotites controlled by fluid character using harzburgites from Rudnik as the example – Serpentinization or talcization? *Serbian Geological Society, Belgrade, Serbia, Report for the Year 2019*:15–26
- Popović R, Umeljić G (2015) Metallogeny of the Rudnik mountain, position in time and space [Original title: Metalogenija planine Rudnik, pozicija u vremenu i prostoru]. *Povremena izdanja*

- Rudnik i flotacija 'Rudnik' doo Rudnik, Beograd, 224 ISBN: 978-86-918511-0-1
- Richards JP (2015) Tectonic, magmatic, and metallogenic evolution of the Tethyan orogen: From subduction to collision. *Ore Geol Rev* 70:323–345
- Roedder E (1984) Fluid inclusions. *Reviews in mineralogy. Mineral Soc America* 12:644. <https://doi.org/10.1515/9781501508271>
- Roedder E, Bodnar RJ (1980) Geologic pressure determinations from fluid inclusion studies. *Annu Rev Earth Planet Sci* 8(1):263–301
- Samson IM, Williams-Jones AE, Ault KM, Gagnon JE, Fryer BJ (2008) Source of fluids forming distal Zn-Pb-Ag skarns: Evidence from laser ablation–inductively coupled plasma–mass spectrometry analysis of fluid inclusions from El Mochito. *Honduras Geology* 36(12):947–950
- Schwinn G, Wagner T, Baatartsogt B, Markl G (2006) Quantification of mixing processes in ore-forming hydrothermal systems by combination of stable isotope and fluid inclusion analyses. *Geochim Cosmochim Acta* 70(4):965–982
- Seghedi I, Downes H, Szakács A, Mason PR, Thirlwall MF, Roşu E, Pécskay Z, Márton E, Panaiotu C (2004) Neogene-Quaternary magmatism and geodynamics in the Carpathian-Pannonian region: a synthesis. *Lithos* 72(3–4):117–146
- Shimazaki H (1982) The Sasano hastingsite-bearing copper skarn deposit formed in aluminous sediment, at the Yoshioka mine. *Japan Econ Geol* 77(4):868–876
- Shu Q, Chang Z, Hammerli J, Lai Y, Huizenga JM (2017) Composition and evolution of fluids forming the Baiyinnuo'er Zn-Pb skarn deposit, northeastern China: Insights from laser ablation ICP-MS study of fluid inclusions. *Econ Geol* 112(6):1441–1460
- Shu Q, Chang Z, Mavrogenes J (2021) Fluid compositions reveal fluid nature, metal deposition mechanisms, and mineralization potential: An example at the Haobugao Zn-Pb skarn, China. *Geology* 49:473–477
- Šoštarić SB, Palinkaš LA, Neubauer F, Hurai V, Cvetković V, Roller-Lutz Z, Mandić M, Genser J (2013) Silver-base metal epithermal vein and listwanite hosted deposit Crnac, Rogozna Mts., Kosovo, part II: A link between magmatic rocks and epithermal mineralization. *Ore Geol Rev* 50:98–117
- Stojanović J, Radosavljević-Mihajlović A, Radosavljević S, Vuković N, Pačevski A (2016) Mineralogy and genetic characteristics of the Rudnik Pb-Zn/Cu, Ag, Bi, W polymetallic deposit (Central Serbia)—New occurrence of Pb (Ag) Bi sulfosalts. *Periodico Di Mineralogia* 85:121–135
- Stojanović JN, Radosavljević SA, Tošović RD, Pačevski AM, Radosavljević-Mihajlović AS, Kašić VD, Vuković NS (2018) A review of the Pb-Zn-Cu-Ag-Bi-W polymetallic ore from the Rudnik orefield, Central Serbia. *Geološki Anali Balkanskoga Poluostrva* 79:47–69
- Storre B (1970) Stabilitätsbedingungen Grossular-führender Paragenesen im System CaO-Al₂O₃-SiO₂-CO₂-H₂O. *Contrib Mineral Petrol* 29(2):145–162
- Sun QF, Wang KY, Wang YC, Yang H, Li J, Ma XL (2021) Fluid evolution and ore genesis of the Chaobuleng skarn Fe-Zn polymetallic deposit, Northeast China: evidence from fluid inclusions, C-O-S-Pb isotopes, and geochronology. *J Geochem Explor* 227:106796
- Tošović R (2000) Genetic and geological-economic modeling of the Rudnik polymetallic deposit. [Original title: Genetsko i geološko-ekonomsko modeliranje polimetaličnog ležišta Rudnik in Serbian]. Dissertation, University of Belgrade, Faculty of Mining and Geology, Belgrade, Serbia
- Ustaszewski K, Kounov A, Schmid SM, Schaltegger U, Krenn E, Frank W, Fügenschuh B (2010) Evolution of the Adria-Europe plate boundary in the northern Dinarides: From continent-continent collision to back-arc extension. *Tectonics* 29(6):TC6017, pp34
- Vidal CCE, Injoke-Espinoza J, Sidder GB, Mukasa SB (1990) Amphibolitic Cu-Fe skarn deposits in the central coast of Peru. *Econ Geol* 85(7):1447–1461
- Whitney DL, Evans BW (2010) Abbreviations for names of rock-forming minerals. *Am Mineral* 95(1):185–187
- Wilkinson JJ (2001) Fluid inclusions in hydrothermal ore deposits. *Lithos* 55(1–4):229–272
- Xie L, Wang Z, Wang R, Zhu J, Che X, Gao J, Zhao X (2018) Mineralogical constraints on the genesis of W-Nb-Ta mineralization in the Laiziling granite (Xianghualing district, south China). *Ore Geol Rev* 95:695–712
- Yang K, Bodnar RJ (1994) Magmatic-hydrothermal evolution in the “Bottoms” of porphyry copper systems: Evidence from silicate melt and aqueous fluid inclusions in granitoid intrusions in the Gyeongsang basin. *South Korea Int Geol Rev* 36(7):608–628
- Zucchi M, Tursi F, Brogi A, Liotta D, Spiess R, Caggianelli A, Ventruti G, Langone A (2023) Syn-tectonic contact aureole and metasomatic reaction zones in carbonate and pelitic host rocks (Elba Island, Italy). *Tectonophysics* 853(229782):22
- Zhang D, Audétat A (2018) Magmatic-hydrothermal evolution of the barren Huangshan pluton, Anhui Province, China: a melt and fluid inclusion study. *Econ Geol* 113(4):803–824
- Zhao CT, Sun JG, Chu XL, Qin KZ, Ren L, Xu Z, Zhi K, Liu J, Han J, Bai C, Shu W (2021) Metallogeny of the Ergu Fe-Zn polymetallic deposit, central Lesser Xing'an Range, NE China: evidence from skarn mineralogy, fluid inclusions and HOS-Pb isotopes. *Ore Geol Revs* 135:104227
- Zhong J, Chen YJ, Pirajno F, Chen J, Li J, Qi JP, Li N (2014) Geology, geochronology, fluid inclusion and H-O isotope geochemistry of the Luoboling porphyry Cu-Mo deposit, Zijinshan Orefield, Fujian Province, China. *Ore Geol Rev* 57:61–77
- Zhou Z, Mao J, Che H, Ouyang H, Ma X (2017) Metallogeny of the Handagai skarn Fe-Cu deposit, northern Great Xing'an Range, NE China: Constraints on fluid inclusions and skarn genesis. *Ore Geol Rev* 80:623–644

Publisher's Note Springer Nature remains neutral with regard to jurisdictional claims in published maps and institutional affiliations.

Springer Nature or its licensor (e.g. a society or other partner) holds exclusive rights to this article under a publishing agreement with the author(s) or other rightsholder(s); author self-archiving of the accepted manuscript version of this article is solely governed by the terms of such publishing agreement and applicable law.